

## Metal-poor Stars Observed with the Southern African Large Telescope

Kaitlin C. Rasmussen<sup>1,2,3</sup>, Joseph Zepeda<sup>1,2</sup>, Timothy C. Beers<sup>1,2</sup>, Vinicius M. Placco<sup>1,2,4</sup>, Éric Depagne<sup>5</sup>,

Anna Frebel<sup>2,6</sup>, Sarah Dietz<sup>1,2</sup>, and Tilman Hartwig<sup>7,8,9</sup>,

1 Department of Physics, University of Notre Dame, Notre Dame, IN 46556, USA

2 JINA Center for the Evolution of the Elements (JINA-CEE), USA; tbeers@nd.edu

3 Department of Astronomy, University of Michigan, 1085 S. University Avenue, Ann Arbor, MI:48109, USA

4 NSF's Optical-Infrared Astronomy Research Laboratory, Tucson, AZ 85719, USA

5 South African Astronomical Observatory (SAAO), Observatory Road Observatory Cape Town, WC 7925, South Africa

6 Department of Physics and Kavli Institute for Astrophysics and Space Research, Massachusetts Institute of Technology, Cambridge, MA 02139, USA

7 Institute for Physics of Intelligence, School of Science, The University of Tokyo, Bunkyo, Tokyo 113-0033, Japan

8 Kavli IPMU (WPI), UTIAS, The University of Tokyo, Kashiwa, Chiba 277-8583, Japan

9 Department of Physics, School of Science, The University of Tokyo, Bunkyo, Tokyo 113-0033, Japan

8 Received 2020 August 13; revised 2020 September 23; accepted 2020 October 8; published 2020 December 8

## **Abstract**

We present the first release of a large-scale study of relatively bright (V < 13.5) metal-poor stars observed with the Southern African Large Telescope (SALT), based on high-resolution spectra of 50 stars with a resolving power of  $R \sim 40,000$  and  $S/N \sim 20$  per pixel at 4300 Å. The elemental abundances of C, Sr, Ba, and Eu are reported, as well as several  $\alpha$ -elements (Mg, Ca, Sc, Ti, and V) and iron-peak elements (Mn, Co, Ni, and Zn). We find a diverse array of abundance patterns, including several consistent with the signatures of carbon-enhanced metal-poor CEMP-i and CEMP-r stars. We find that 15 of 50 (30%) are carbon enhanced (with [C/Fe] > +0.70), and that a large fraction (26 of 50, 52%) are enhanced in r-process elements. Among the r-process-enhanced stars, five are strongly enhanced r-II ([Eu/Fe] > +1.0) stars (two of which are newly discovered) and 21 are newly discovered moderately enhanced r-I ( $+0.3 \le [Eu/Fe] \le +1.0$ ) stars. There are eight stars in our sample that, on the basis of their abundances and kinematics, are possible members of the metal-weak thick-disk population. We also compare our measured abundances to progenitor-enrichment models, and find that the abundance patterns for the majority of our stars can be attributed to a single (rather than multiple) enrichment event.

*Unified Astronomy Thesaurus concepts:* Stellar nucleosynthesis (1616); Explosive nucleosynthesis (503); Milky Way stellar halo (1060); Stellar abundances (1577); Stellar dynamics (1596)

Supporting material: machine-readable tables

## 1. Introduction

Metal-poor stars are the oldest survivors of the earliest era of star formation after the Big Bang; they preserve material in their photospheres that has (with the exception of mass-transfer binaries) remained essentially unaltered since their birth (Beers et al. 1992 and references therein). This allows for the direct examination of star formation environments that have not existed for billions of years. Their frequencies, elemental abundances, and kinematics provide insight into early star formation channels, nucleosynthesis pathways, and Galactic assembly. As such, they are a valuable tool for studying many facets of the early universe.

Metal-poor stars exhibit diverse elemental-abundance patterns; it is thus useful to define several subclasses. Stars that are over-abundant in carbon relative to iron, compared to the solar ratio ( $[{\rm C/Fe}]^{10} > +0.70$ ), are referred to as carbon-enhanced metal-poor (CEMP) stars. Stars that are also over-abundant in the neutron-capture elements are referred to as CEMP-s, CEMP-i, or CEMP-r, depending on their overall heavy element-abundance patterns. The CEMP-no stars exhibit under-abundances of neutron-capture elements relative to the solar ratios. Quantitative abundance definitions can be found in Table 1, adapted from Beers & Christlieb (2005) and Frebel (2018).

At very low metallicities, the presence of large amounts of carbon relative to iron is significant because it a strong indicator that a star likely formed in the early universe through cooling channels involving C II and/or O I (Bromm & Loeb 2003; Frebel et al. 2007). This is supported by the observed increase in the cumulative fraction of CEMP stars that have not been externally enriched by a mass-transfer event from a binary companion (i.e., CEMP-no and CEMP-r), as demonstrated in Lee et al. (2013), Placco et al. (2014), and Yoon et al. (2018). According to the most recent work, this fraction grows steadily from  $\sim$ 30% at [Fe/H] < -2.5 to  $\sim$ 100% at [Fe/H] < -4.5. The search for CEMP-no stars is thus important, since these stars have the greatest potential to represent bona fide second-generation stars.

The presence of the (predominantly) *r*-process element Eu in a very metal-poor star (along with [Ba/Eu] < 0, to exclude possible *s*- or *i*-process contributions) indicates that an explosive progenitor event, such as a neutron star merger (Lattimer & Schramm 1974; Arcones et al. 2007; Thielemann et al. 2017), likely enriched the star's natal cloud with significant amounts of heavy elements beyond the iron peak. Specifically, the *r*-process-element abundance patterns (strictly speaking, the residuals from the solar pattern after subtracting the *s*-process contribution, e.g., Burris et al. 2000) of such stars encode unique information on the nature of the possible astrophysical sites and the various nucleosynthetic pathways involved in the operation of the *r*-process.

In addition to C and Eu, several other elemental abundances can be useful tests of first-star and Galactic chemical-evolution

 $<sup>\</sup>overline{^{10}}$  Relative abundance ratios used in this work correspond to  $[A/B] = \log(N_A/N_B) - \log(N_A/N_B)_{\odot}$ , where *N* indicates the number density of the given species.

**Table 1**Metal-poor Subclass Definitions

Subclasses	Definition				
	r-process-enhanced stars				
r-I	$0.3 \leq [Eu/Fe] \leq +1.0, [Ba/Eu] < 0$				
r-II	$[\mathrm{Eu}/\mathrm{Fe}] > +1.0, [\mathrm{Ba}/\mathrm{Eu}] < 0$				
	Carbon-enhanced metal-poor stars				
CEMP	[C/Fe] > +0.7				
CEMP-r	[C/Fe] > +0.7, [Eu/Fe] > +1.0				
CEMP-s	[C/Fe] > +0.7, [Ba/Fe] > +1.0, [Ba/Eu] > +0.5				
CEMP-i	[C/Fe] > +0.7, 0.0 < [Ba/Eu] < +0.5 (-1.0 < [Ba/Pb]				
	<-0.5)				
CEMP-no	[C/Fe] > +0.7, [Ba/Fe] < 0				

models (e.g., Côté et al. 2016, 2017 and references therein). Measurements of  $\alpha$ -capture elements, such as Mg, can be used to between models for first-star nucleosynthesis mechanisms (Yoon et al. 2016 and references therein), as well as to separate stars with single supernova progenitors from those with multiple supernova progenitors (Hartwig et al. 2018). Other neutron-capture element abundances, such as Ba, can provide insights into the s-process operating in the asymptotic giant branch (AGB) stars and the subsequent mass transfer across a binary system (Herwig 2005; Bisterzo et al. 2010; Abate et al. 2015), or in massive, rapidly rotating extremely low-metallicity stars (e.g., Pignatari et al. 2008; Meynet et al. 2010; Maeder et al. 2015; Choplin et al. 2016, 2018), as well as the possible operation of the *i*-process, the astrophysical site(s) for which are still under investigation (Hampel et al. 2016; Denissenkov et al. 2017).

## 2. Target Selection and Observations

## 2.1. Target Selection

The stars that comprise this sample are the first data release from a total of  $\sim 200$  metal-poor stars, selected from candidates identified during the Radial Velocity Experiment (RAVE) survey (Steinmetz et al. 2006; Kunder et al. 2017). RAVE obtained moderate-resolution ( $R \sim 7500$ ) spectroscopy of bright stars in the region of the Ca triplet, and derived stellar parameters ( $T_{\rm eff}$ , log g, and [Fe/H]) and abundance estimates for a limited number of elements. Their sample of nearly 500,000 stars was selected on apparent magnitude, effectively removing the biases typically associated with searches for metal-poor stars, such as selection on metallicity itself, kinematics, coverage of a limited range of evolutionary status, or membership in a specific Galactic population.

To arrive at the current sample, medium-resolution ( $R \sim 2000$ ) spectra of candidate metal-poor RAVE stars were obtained (see Figure 1), and processed by the non-SEGUE Stellar Parameter Pipeline (n-SSPP; Beers et al. 2013, 2017), which compares observed spectra to synthetic spectra to predict [C/Fe], along with their stellar atmospheric parameters ( $T_{\rm eff}$ , log g, and [Fe/H]), using a number of approaches (Placco et al. 2018). The estimates of [C/Fe] were then corrected for evolutionary effects, as discussed by Placco et al. (2014), in order to better approximate their natal C abundances.

The full sample of  $\sim\!200$  SALT stars were selected after this step on the basis of brightness and/or their high [C/Fe] abundances, to maximize the numbers of likely CEMP stars in the sample. The sample of 50 stars reported on here were

picked from the full sample as a pilot study. This pilot sample covers the same apparent magnitude range as the full  $\sim 200$  star sample (see Figure 2).

## 2.2. SALT Observations

A total of 55 hr of observing time was granted at the 11 m Southern African Large Telescope (SALT; Buckley et al. 2006) for the Long Term Proposal 2017-1-MLT-012, "Detailed Study of CEMP Stars Identified in the RAVE Survey." The observations were carried out in service mode during four consecutive semesters, beginning in 2017 April and ending in 2019 March. A total of 223 stars were observed with the High Resolution Spectrograph (HRS; Bramall et al. 2010, 2012; Crause et al. 2014) at a resolving power of  $R \sim 40,000$ . Examples of several of the important absorption features are shown in Figure 3.

The HRS is a dual-beam, single-object, fiber-fed echelle spectrograph that utilizes a pair of fibers to simultaneously image a target and the nearby sky background. It employs volume phase holographic (VPH) gratings composed of dichromated gelatin between two optical windows as cross-dispersers. HRS has three resolution settings ( $R \sim 14,000, R \sim 40,000$ , and  $R \sim 65,000$ ), which deliver light to one blue (370–550 nm) 2k by 4k CCD chip and one red (550-890 nm) 4k by 4k fringesuppressing deep-depletion chip. Nominal exposure times were  $\sim$ 2 h, depending on the brightness of the target, leading to a typical signal-to-noise ratio (S/N) of  $\sim$ 20 per pixel at 4300 Å. The useful wavelength range of the spectra is 3990-5560 Å, as the signal is dominated by the noise blueward of 3990 Å, and issues within our own reduction pipeline made reduction of the red wing infeasible. Further observing details can be found in Table 2.

## 3. Data Analysis and Stellar Parameters

### 3.1. Data Reduction

Reduction of the raw spectra from HRS was carried out with a custom-made code designed for SALT spectra utilizing IRAF routines (Tody & Crawford 1986; Tody et al. 1993). The packages noao, imred, cddred, and echelle were employed, specifically, using the tasks *ccdproc*, *imcombine*, *apflatten*, *apscatter*, and *apall*.

Spectra were normalized, stitched together, and radial-velocity corrected with the software Spectroscopy Made Hard (SMH; Casey 2014), which is a python wrapper of the FORTRAN-based MOOG routine (Sneden 1973; Sobeck et al. 2011). Atomic data for the absorption lines used for equivalent-width determination are listed in the Appendix.

#### 3.2. Stellar Parameters

Effective-temperature estimates were determined by minimizing trends between the abundances of Fe I lines and their excitation potentials, and applying the temperature correction from the spectroscopic to the photometric scale suggested by Frebel et al. (2013). The microturbulent velocity was determined by minimizing the trend between the abundances of Fe I lines and their reduced equivalent widths (REW;  $\log(\text{Eq.Width})/\lambda_o$ ). The surface gravity was determined from the balance of the two ionization stages of iron, Fe I and Fe II. The derived atmospheric parameters for our sample are listed in Table 4. The location of the stars in our sample along isochrones generated for

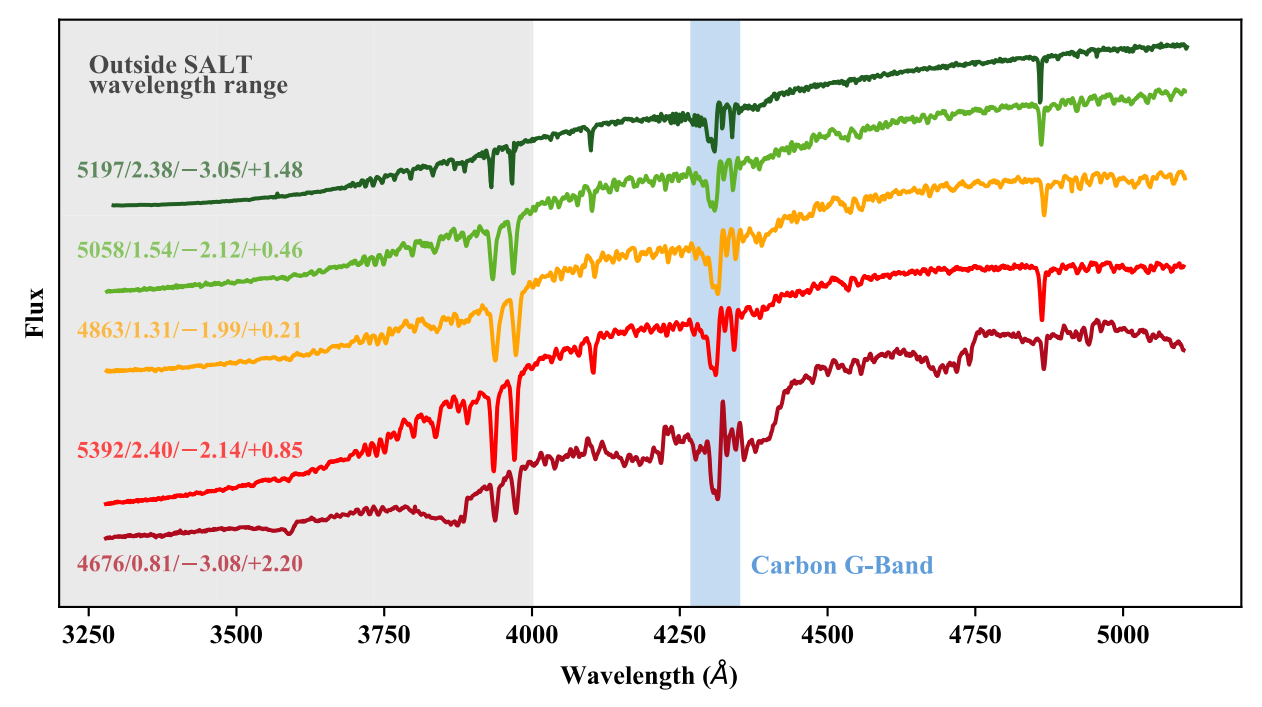


Figure 1. Medium-resolution ( $R \sim 2000$ ) spectra of several stars in our sample. Estimates of  $T_{\rm eff}/\log g/[{\rm Fe/H}]/[{\rm C/Fe}]$  obtained by the n-SSPP are shown for each star: J153830.9–180424 (light green), J100709.2–180947 (orange), J061950.0–531212 (red), and J044208.2–342114 (dark red) were taken with the EFOSC2 spectrograph at the New Technology Telescope (NTT), while J222236.0–013827 (dark green) was taken with the RCSPEC spectrograph at the Mayall 4 m Telescope. The gray region on the left indicates the wavelength range not covered by the high-resolution SALT spectra. The blue shaded region indicates the location of the CH G-band used by the n-SSPP to estimate  $[{\rm C/Fe}]$ . The values of  $[{\rm C/Fe}]$  shown have been corrected for evolutionary effects, as discussed by Placco et al. (2014).

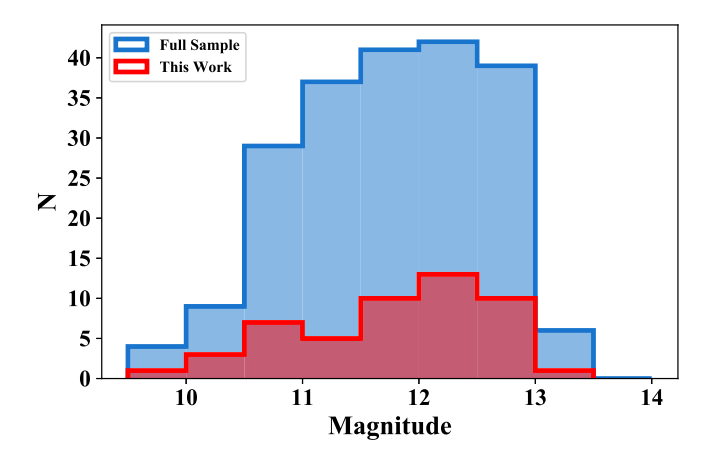


Figure 2. Distribution of V magnitudes for the present sample, as well as for the complete set of  $\sim$ 200 stars observed with SALT on this program.

 $[\mathrm{Fe/H}] = -1.0$ , -2.0, and -3.0 for both 10 and 12 Gyr, based on their derived atmospheric parameters, is shown in Figure 4. There is little difference between the 10 and the 12 Gyr isochrones for post-main-sequence stars, but it is instructive to show that the sample matches what we expect to see for a population of old, metal-poor stars.

#### 3.3. Comparison with Prior Estimates

Temperature. Figure 5 shows a comparison of effective-temperature estimates for our stars. For stars with RAVE DR4 results (Kordopatis et al. 2013), there is only moderate agreement between the reported temperatures and the temperatures derived in this work (Figure 5). RAVE DR5 (Kunder et al. 2017) only issued corrections for stars above 6000 K, which does not affect the

majority of our generally cooler stars. However, new RAVE DR5 temperatures based on IR photometry exhibit far better agreement with our results, as do the temperatures derived from the n-SSPP.

Surface Gravity. Surface gravity (see Figure 6) is often difficult to accurately estimate, even with high-resolution spectra. For both RAVE DR4 and DR5, the scatter with respect to our results is quite large, and  $\log g$  is frequently overestimated by nearly a dex. Better agreement is achieved with the n-SSPP values, but the spread is still rather large.

Metallicity. Figure 7 shows a comparison of derived metallicities. The metallicities from RAVE DR4 exhibit a rather large scatter compared with our SALT determinations, and include a number of highly deviant stars at the lowest [Fe/H]; the scatter and deviant behavior is reduced for RAVE DR5. The scatter compared to the n-SSPP is generally good, but there remain a number of stars with significant deviations. Many of these outliers have either high carbon abundances (A(C) > 7.35), lower temperature ( $T_{\rm eff} < 4750~{\rm K}$ ), or both. This is a known difficulty for medium-resolution spectra analyzed with the n-SSPP, due in part to the nascent saturation of the CH G-band, and the depression of the continuum by molecular carbon veiling in the region of the Ca II K line, which is a primary metallicity estimator for that routine. An improved methodology for dealing with both of these challenges has been recently developed, and is reported on by Yoon et al. (2020).

#### 4. Chemical Abundances

The elements C, Mg, Ca, Sc, Ti, V, Cr, Mn, Fe, Co, Ni, Zn, Sr, Ba, and Eu have been measured (or had upper limits determined) for all 50 stars in our data set. Metallicity ranges from [Fe/H] = -2.92 to -0.94, with typical values around  $[Fe/H] \sim -2.40$ . Abundances of all elements, except for C, Sr, Ba, and Eu, were measured using the equivalent-width approach.

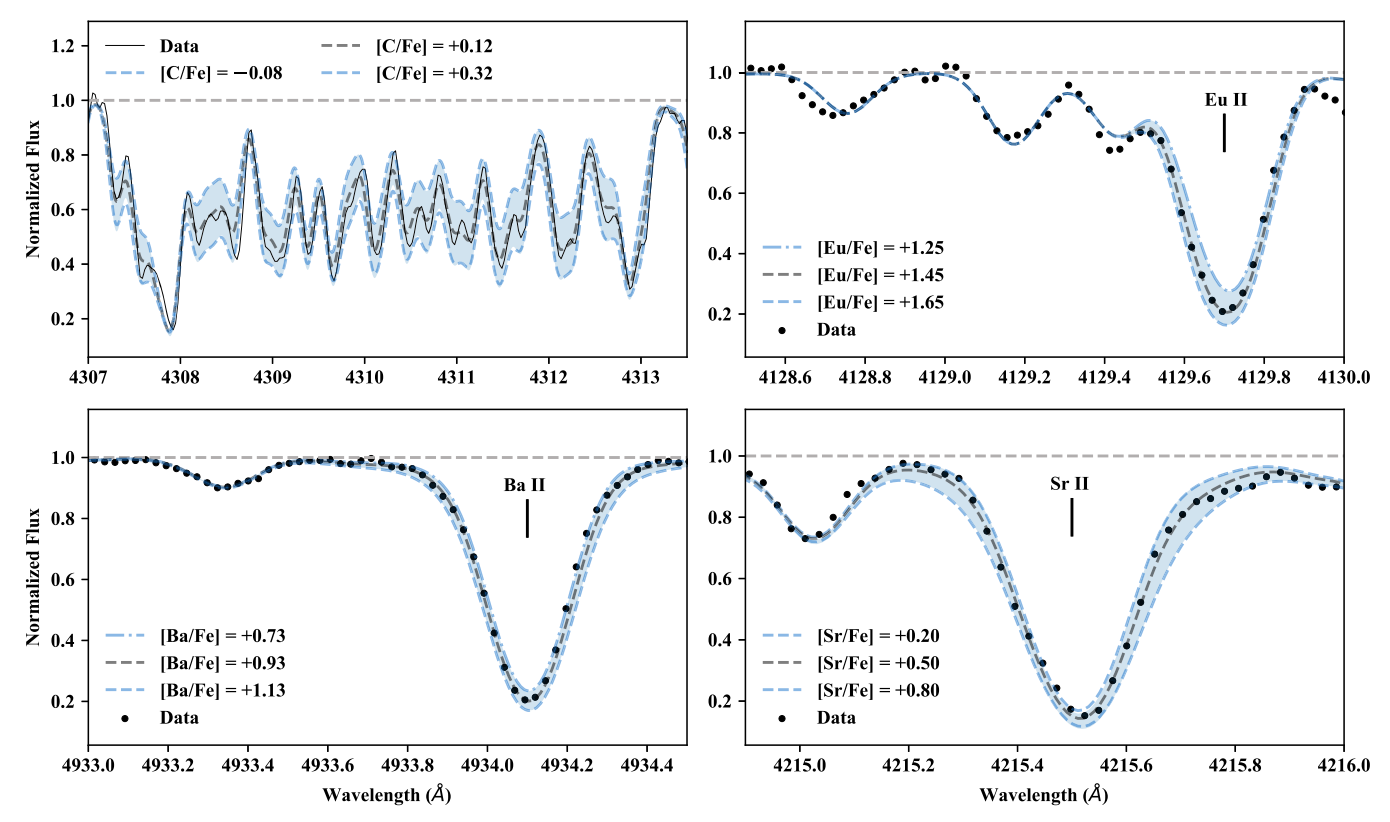


Figure 3. Comparison of high-resolution data with synthetic spectra for the elements carbon, europium, barium, and strontium, for the r-II star J153830.9-180424. The black dots indicate the observed spectra, while the blue shaded region indicates the range around the best-fit values, as provided in the legend for each panel. Top left: the CH G-band at  $\sim \lambda 4310$  Å. Top right: the Eu II line at  $\lambda 4129$  Å. Bottom left: the Ba II line at  $\lambda 4934$  Å. Bottom right: the Sr II line at  $\lambda 4215$  Å.

Gaussian profiles were fit to all absorption lines in our line list to obtain the line measurements. We applied an REW cutoff of -4.5, as this is the point above which equivalent widths no longer linearly correlate with increasing abundance. Uncertainties for these element abundances are reported as the standard deviation resulting from multiple measurements. In the case of single-line measurements, we adopt a nominal value of  $0.10 \, \mathrm{dex}$ . In the case of any synthesized spectral features, the uncertainty is chosen to represent the difference between the best-fit abundances and a synthetic spectrum with an abundance that encapsulates all of the data points across the region of the line. Example spectra can be found in Figure 3.

The derived abundances of elements useful for classifying our program stars, as discussed above, are listed in Table 5. Comparison of these abundances (and the adopted atmospheric parameters) for nine of our stars with previous high-resolution spectroscopic analyses are listed in Table 3. We find that our carbon and barium values are largely consistent between works when uncertainties and differing temperatures are taken into account, and that Sr and Eu are mostly consistent, with a few outliers. For Sr, inconsistencies are likely to come from the large depth of the line combined with its many blends; for Eu, inconsistencies beyond measurement uncertainty arise when the [Eu/Fe] ratio is high and the line begins to saturate.

Additional elemental abundances for our program stars are listed in Table 6 ( $\alpha$ -elements), and Table 7 (iron-peak elements), and are described briefly below.

## 4.1. Carbon and the $\alpha$ -Elements

Carbon abundances were measured using spectral synthesis of the CH G-band at  $\lambda$ 4313 Å. The great majority of the stars in

our sample are red giants, so we assume an equilibrium isotopic ratio value of  $^{12}\text{C}/^{13}\text{C}\sim 5.0$ . These giants have experienced a varying degree of internal carbon depletion due to CN processing. To correct for this depletion, the procedure from Placco et al. (2014) was applied. Corrected C abundances are reported in Table 5 as  $[\text{C/Fe}]_{\text{corr}}$ .

Mg I abundances were measured using lines redward of  $\lambda4000\,\text{Å}$ , including the Mg triplet, when an REW of less than -4.5 was reported. Ca I was measured in a similar fashion. No Ca II lines were available within our wavelength range. Sc I lines, at these metallicities and S/N, and within the available wavelength range, are too weak to measure; we instead report abundances based on as many as eight Sc II lines. We measure both Ti I and Ti II species, and report their abundances individually. The results for these elements are listed in Table 6.

## 4.2. Iron-peak Elements

For our data, a reliable V I abundance is reported based on only a single line at  $\lambda4786.50\,\text{Å}$ . Both Cr I and Cr II abundances are reported when the S/N is sufficiently high to measure the three weak Cr II lines at  $\lambda4558.59\,\text{Å}$ ,  $\lambda4588.14\,\text{Å}$ , and  $\lambda4591.99\,\text{Å}$ . Between 60 and 80 lines were measured for Fe I, and 5 to 15 for Fe II, depending on the temperature, metallicity, and S/N of the stellar spectrum.

Mn I and Ni I abundances are measured from 7 and 18 lines, respectively. Because the majority of Co I lines lie blueward of  $\lambda4000\,\text{Å}$ , we derive its abundance from only the one line at  $\lambda4121.32\,\text{Å}$ . Zn I is measured from the two lines at  $\lambda4722.15\,\text{Å}$  and  $\lambda4810.53\,\text{Å}$ . The results for these elements are reported in Table 7.

Table 2
Details of the Observations

Name	Obs. Date	Exp. Time (hr)	S/N @ 4310 Å	V
RAVE J012931.1-160046 <sup>a</sup>	2017 Jun 11	2.65	23	11.64
RAVE J030639.1-692040	2018 Jul 21	1.75	15	12.36
RAVE J035550.9-721151	2017 Jun 13	1.95	20	13.35
RAVE J040618.2-030525	2017 Oct 28	1.80	19	12.17
RAVE J044208.2-342114 <sup>b</sup>	2017 Oct 26	2.25	18	11.65
RAVE J045322.6-221040 <sup>c</sup>	2017 Oct 26	1.60	25	10.66
RAVE J053817.0-751621	2017 Nov 5	2.20	21	11.21
RAVE J061950.0-531212	2017 Oct 26	1.90	18	11.37
RAVE J071234.0-481405	2017 Apr 9	2.90	21	11.57
RAVE J074824.3-483141	2017 Apr 21	2.25	28	11.29
RAVE J100709.2-180947	2017 Dec 5	1.70	14	12.36
RAVE J111711.0-310951	2017 Apr 22	1.60	14	11.56
RAVE J111912.3-160947	2017 Apr 10	2.00	26	12.37
RAVE J113508.3-111328	2017 Apr 14	1.50	15	12.70
RAVE J114444.8-112817	2017 Apr 10	1.55	42	9.80
RAVE J115941.7-382043	2017 Apr 16	1.25	20	12.26
RAVE J123550.1-313111	2017 Apr 17	2.00	10	10.70
RAVE J124154.7-085701	2018 Feb 7	2.80	16	12.06
RAVE J124753.3-390802	2018 Jan 14	2.45	10	12.23
RAVE J130524.5-393126	2017 Apr 17	1.70	14	12.82
RAVE J132141.8-432006	2017 May 6	2.35	17	11.42
RAVE J132414.3-180620	2017 May 3	2.30	22	11.41
RAVE J134319.3-235814	2017 May 11	2.50	22	11.56
RAVE J151558.3-203821	2017 Apr 19	2.30	26	11.64
RAVE J151608.7-212160	2017 May 3	2.75	14	10.85
RAVE J153539.5-173455	2017 Apr 16	2.25	15	12.14
RAVE J153830.9–180424 <sup>d</sup>	2017 May 12	1.85	25	10.86
RAVE J154230.9–210731	2017 Apr 17	2.30	16	12.53
RAVE J155829.6–122434	2017 Apr 17	2.20	17	12.33
RAVE J160245.0–152102 <sup>e</sup>	2017 Apr 18	1.50	30	10.35
RAVE J165300.5-005507	2017 Apr 18 2017 May 17	2.15	20	12.68
RAVE J171633.4-700902	2017 May 17 2019 Mar 22	2.85	12	10.48
RAVE J171033.4-700902 RAVE J175159.8-475131	2019 Mai 22 2019 Feb 22	2.00	17	10.48
RAVE J175139.8–475131 RAVE J180242.3–440443 <sup>e</sup>	2019 Jun 12	2.30	14	12.62
RAVE J180242.3—440443 RAVE J183108.2—491105	2018 Jul 12 2018 Jul 22	2.10	14	12.86
RAVE J183623.2-642812	2018 Jun 24	2.35	15	12.45
RAVE J183023.2-042812 RAVE J191755.9-544015	2017 Oct 27	2.05	25	10.76
RAVE J192632.8–584657	2017 Oct 27 2017 Apr 16	2.95	17	12.52
RAVE J192032.8-384037 RAVE J192819.9-633935	2017 Apr 10 2017 May 18	1.85	18	12.76
	2017 May 18 2017 May 5	1.90	21	12.76
RAVE J194550.6—392631	2017 May 3 2018 Jun 24	1.75	13	12.20
RAVE J201446.1–563530 RAVE J203706.4–122125	2018 Jul 18	2.63	22	11.69
RAVE J204450.7-371400 RAVE J204954.4-480045	2018 Jun 25	3.30	22	12.35
RAVE J204954.4—480045 RAVE J205149.7—615801	2017 Oct 27	1.65	28	11.86 12.31
	2017 May 16	1.55 1.95	21	
RAVE J205609.1—133118 <sup>e</sup>	2017 May 6	1.55	25 22	10.19 12.80
RAVE J210642.9—682827 <sup>e</sup>	2018 Jun 25			
RAVE J211413.5-572636	2017 Apr 22	2.65	16	10.54
RAVE J215118.3–135937 RAVE J222236.0–013827 <sup>i</sup>	2017 Nov 5	1.50 2.25	16 16	11.93
MAYE J222230.0-013027	2018 Jul 7	2.23	10	11.87

**Note.** A handful of these stars have been previously observed in other programs since the beginning of the observing campaign or earlier and are noted as such: (a) Hansen et al. (2015), (b) Sakari et al. (2018b), (c) Sakari et al. (2018a), (d) Hansen et al. (2018), and (e) Roederer et al. (2014). Their stellar atmospheric parameters and [C/Fe], [Sr/Fe], [Ba/Fe], and [Eu/Fe] values are compared in Table 3.

## 4.3. Neutron-capture Elements

Estimates of the elemental abundances for Sr, Ba, and Eu have been handled with extra care, as they are the elements by which our program metal-poor stars are classified. Details for each element are provided below.

Strontium. The Sr II abundance was measured from the  $\lambda$ 4215 Å line, as it is quite strong and does not easily oversaturate,

unlike the line at  $\lambda 4077$  Å. The  $\lambda 4161$  Å line is weak and closer to the blue cutoff, so it was inaccessible in most cases.

*Barium.* Ba II was measured from the  $\lambda 4934$  Å line, as this feature is strong, accessible, and isolated from blends. It also does not oversaturate, as the 4554 Å is known to in cases of strong *s*-process enhancement.

Europium. Eu II was measured from the  $\lambda$ 4129 Å line, which is strong and accessible. It is blended with a Dy II line;

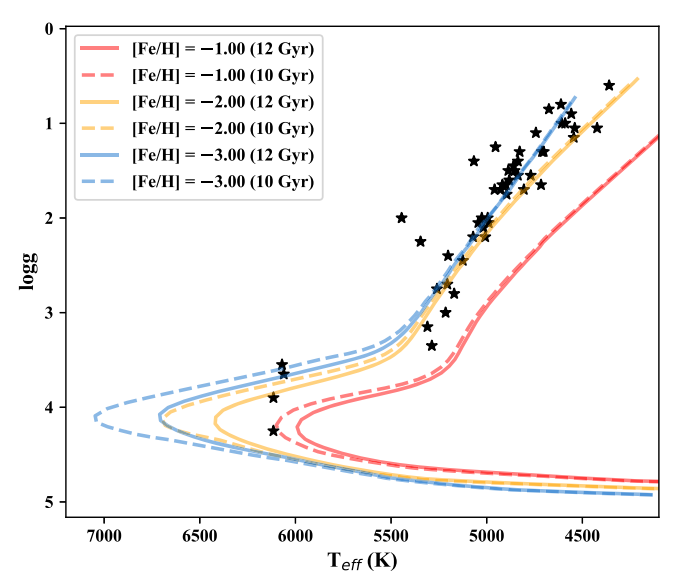


**Figure 4.** Comparison of the program sample to a set of isochrones. The three solid or dashed lines represent isochrones with a common age of either 10 or 12 Gyr, respectively, for metallicities of [Fe/H] = -1.0 (red), -2.0 (orange), and -3.0 (blue). Data used to generate the isochrones were taken from Placco et al. (2019).

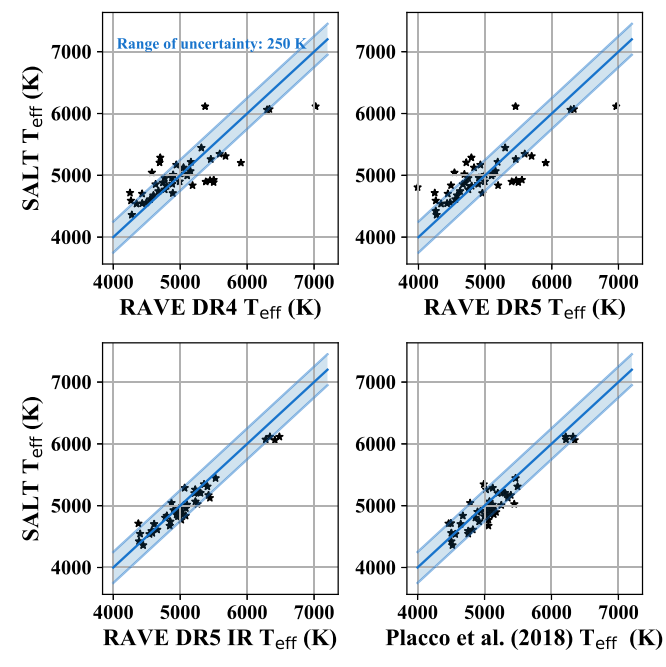


**Figure 5.** Temperatures from RAVE DR4 (top left), RAVE DR5 (top right), RAVE DR5 IR (bottom left), and Placco et al. (2018; bottom right), compared to the atmospheric parameters derived in this work. The blue shaded region marks a  $\pm$  250 K margin of error.

however, these are both r-process elements and reliably scale with one another over a wide range of [Eu/Fe] values. Other Eu lines exist; however, they are largely too weak to be measured at the typical S/N of our spectra.

## 4.4. Comparisons with Prior Abundance Measurements

Nine of our stars have previous estimates of stellar atmospheric parameters and chemical abundances based on high-resolution spectroscopy, the majority of which originate from the *R*-process Alliance data releases (Hansen et al. 2018; Sakari et al. 2018a). These are provided in Table 3. Comparing to the atmospheric parameters and abundances in the present work, we find very good agreement for several stars, while others exhibit moderate disagreements. In those cases, significant differences in  $v_{\rm turb}$  can account for the differences, while for one case, our temperature estimate differs by  $\sim 400~\rm K$ , with respect to that determined on a purely spectroscopic scale by Roederer et al. (2014); this results in large abundance differences. In addition, measurements based on relatively low-S/N spectra result in larger uncertainties for both our work and for several stars in the comparison sample.

## 5. Metal-poor Star Subclassifications and Frequencies

## 5.1. Classifications

We have classified all of our program stars with astrophysically interesting chemical-abundance signatures, in order to assess their frequencies among Galactic halo stars. Over time, as ever larger samples of metal-poor stars with these signatures become available, this should eventually enable detailed assessments of the nucleosynthetic origins of these patterns.

Subclassifications for our program stars have been performed, based on A(C), [C/Fe], [Ba/Fe], and [Eu/Fe], listed along with [Sr/Fe] in Table 5. This is adequate for all but two of our stars, those that are likely CEMP-i stars. Such stars are difficult to classify, because confident membership within the CEMP-i class depends on a Pb abundance, a measurement we cannot obtain from our data. With higher-S/N spectra, the detailed abundance patterns could be established to further verify and fill in the details of the relevant nucleosynthesis signatures.

The distribution of CEMP stars in the A(C)–[Fe/H] fall into at least three groups, as defined in the Yoon-Beers diagram presented by Yoon et al. (2016). Group I is primarily populated by relatively higher-metallicity CEMP-s stars that received their high C abundances through mass transfer from a binary AGB companion. Group II includes stars with a relatively low [Fe/H] and very low A(C) values, which can be classified as CEMP-no stars on the basis of either their A(C) or, when available, low [Ba/Fe] ratios. Group III also contains CEMPno stars, with low [Ba/Fe], but at extremely- to ultra-low metallicities, and with higher A(C) than Group II CEMP-no stars. As argued by Yoon et al. (2016), different progenitor scenarios are thought to be responsible for the production of the stars in Groups II and III. The availability of different cooling channels, as discussed in Chiaki et al. (2017), may also play an important role.

From inspection of the locations of our stars in the Yoon–Beers diagram, shown in Figure 8, five of our CEMP stars fall into Group I, seven into Group II, and three into the region shared by Groups I and II. No stars in our sample have metallicities sufficiently low to be uniquely associated with Group III.

## 5.2. Frequencies of CEMP and r-process-enhanced Stars

We find that 52% of our program stars are enhanced at the [C/Fe] > +0.50 level (using the corrected carbon abundances), 30% of our sample is carbon-enhanced at the [C/Fe] > +0.70 level, and 14% of our sample at the [C/Fe] > +1.00 level. Of the 15 CEMP stars, six are CEMP-no, four are CEMP-s, two are

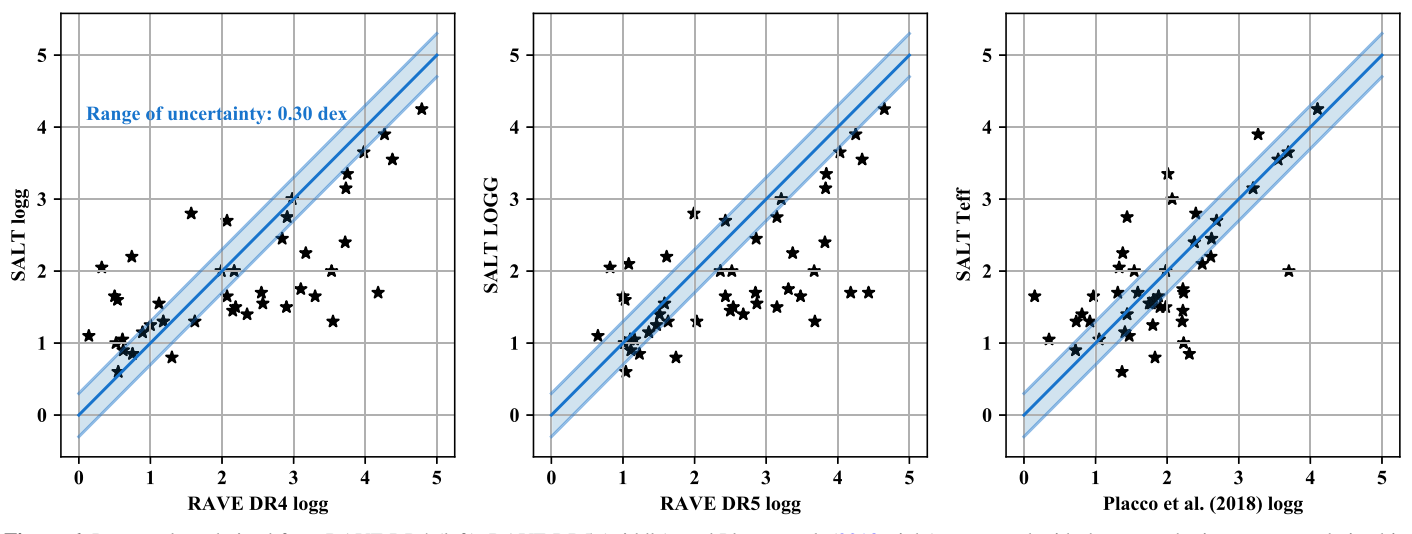


**Figure 6.** Log g values derived from RAVE DR4 (left), RAVE DR5 (middle), and Placco et al. (2018; right), compared with the atmospheric parameters derived in this work. The blue shaded region marks a 0.30 dex margin of error.

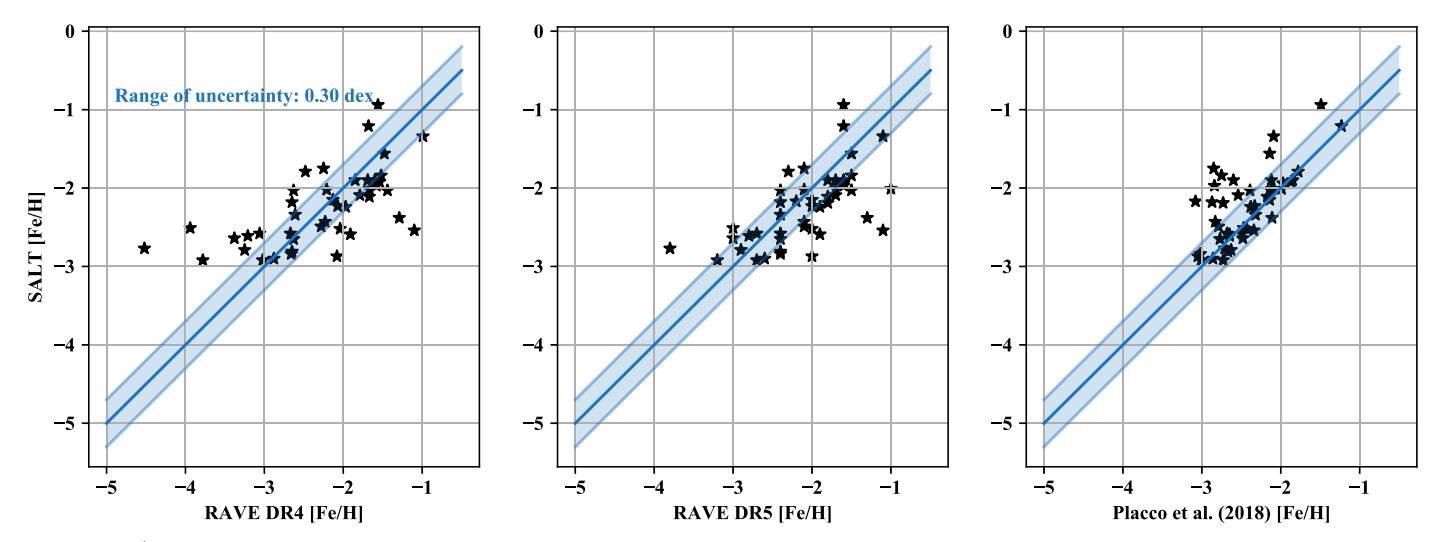


Figure 7. [Fe/H] values reported by RAVE DR4 (left), DR5 (middle), and Placco et al. (2018; right), compared with the atmospheric parameters derived in this work. The blue shaded region marks a 0.30 dex margin of error. Outliers in the Placco et al. (2018) comparison are generally stars that have either a very high A(C) value (A(C) > 7.35), a lower temperature (A(C) = 7.35

likely CEMP-i, and three are CEMP-r stars. Of the CEMP-r stars, one is an r-I, and two are r-II, adding to the small number of such stars that were previously known. RAVE J180242.3 -440443 has  $[C/Fe] = +0.78 \pm 0.25$  with [Eu/Fe] = $+1.20 \pm 0.30$ . [Eu/Fe] has also been measured for this star by Hansen et al. (2018), who reports  $[Eu/Fe] = +1.05 \pm 0.30$ . RAVE J171633.4-700902 has  $[C/Fe] = +0.73 \pm 0.25$ , with  $[Eu/Fe] = +1.09 \pm 0.30$ , but no other previous measurements. A total of 10 CEMP-rII stars are now known, including the canonical r-II star CS 22892-052 (a compilation is provided in D. Guden et al. 2020, in preparation); it appears clear that rprocess enrichment must at least occasionally take place in carbon-enhanced gas, presumably provided by either massive first stars in some of the earliest star-forming regions, or by progenitors that have been suggested to be capable of producing both C during their lifetimes and r-process elements when they explode, such as collapsars (see, e.g., Siegel et al. 2019).

Our sample was selected to be predominantly carbon rich. Accordingly, our CEMP fraction cannot be meaningfully compared to previous literature CEMP fractions. We believe that the reason a CEMP fraction greater than 30% was not actually achieved, as initially intended, is likely due to a temperature offset. This can be seen in the bottom right panel of Figure 5. On average, we arrived at temperatures 100–200 K lower than that obtained by Placco et al. (2018) for their medium-resolution spectra. This has naturally led to lower carbon abundances for the majority of the stars in our sample.

r-process-enhanced stars: half (52%) of the program stars of our sample are enriched in r-process elements, with 21 stars (42%) being classified as r-I and five (10%) classified as r-II. Of the r-II stars, three were either known previously or discovered during the course of the observing campaign by the RPA: CS 31082-001 (Cayrel et al. 2001; Hill et al. 2002), RAVE J180242.3—440443 (Roederer et al. 2014), and RAVE J153830.9—180424 (Sakari et al. 2018b). Two such stars, RAVE J040618.2—030525 and RAVE J171633.4—700902.8, are newly discovered, with  $[\mathrm{Eu}/\mathrm{Fe}] = +1.17 \pm 0.20$  and  $+1.09 \pm 0.30$ , respectively. These frequencies are consistent with the RPA pilot surveys

 Table 3

 Stellar Atmospheric Parameters and Abundances for Previously Observed Stars

Name	Other Name			Literat	ure Values			Thi	s Work	
		Lit.	$T_{\rm eff}$ (K)	log g(cgs)	[Fe/H]	$v_{\rm turb}({\rm km\ s}^{-1})$	$T_{\rm eff}({ m K})$	log g(cgs)	[Fe/H]	$v_{\rm turb}({\rm km~s}^{-1})$
RAVE J012931.1-160046	BPS CS 31082-001	1	4800	1.50	-3.01	1.95	4959	1.70	-2.77	2.65
RAVE J044208.2-342114	HE 0440-3426	2	4800	1.60	-2.20	1.90	4837	1.40	-2.17	2.25
RAVE J045322.6-221040	TYC 5911-452-1	3	6225	4.54	-1.88	2.33	6115	3.90	-2.54	1.60
RAVE J153830.9-180424	TYC 6189-285-1	4	4752	1.63	-2.09	1.51	4995	2.00	-2.02	1.85
RAVE J160245.0-152102	BD -14 4336	5	5240	3.16	-1.80	1.65	5215	3.00	-1.90	1.50
RAVE J180242.3-440443	UCAC2 13007354	5	4701	1.60	-1.55	2.17	4711	1.30	-1.84	2.30
RAVE J205609.1-133118	HD 358059	5	4780	1.60	-2.30	1.80	4918	1.65	-2.24	1.95
RAVE J210642.9-682827	UCAC2 2203606	5	5186	2.70	-2.76	2.90	5026	2.00	-2.92	1.55
RAVE J222236.0-013827	BPS CS 29502-092	6	4820	1.50	-3.20	1.50	5205	2.40	-2.87	2.25
			[C/Fe]	[Sr/Fe]	[Ba/Fe]	[Eu/Fe]	[C/Fe] <sup>a</sup>	[Sr/Fe]	[Ba/Fe]	[Eu/Fe]
RAVE J012931.1-160046	BPS CS 31082-001	1	+0.20	+0.65	+1.17	+1.63	+0.44	+0.96	+1.20	+1.80
RAVE J044208.2-342114	HE 0440-3426	2	+1.51	+0.33	+0.46	<+0.62	+1.44		+0.49	+0.39
RAVE J045322.6-221040	TYC 5911-452-1	3	-0.38	-0.23	-0.68	<- 0.21	< 0.00	-0.29	-0.73	
RAVE J153830.9-180424	TYC 6189-285-1	4	+0.26	+0.44	+0.62	+1.27	+0.12	+0.50	+0.72	+1.52
RAVE J160245.0-152102	BD -14:4336	5	-0.05	+0.35	+0.08	+0.55	+0.14	+0.11	0.00	+0.53
RAVE J180242.3-440443	UCAC2 13007354	5	+0.35	+0.68	+0.95	+1.05	+0.48	+0.15	+0.03	+1.20
RAVE J205609.1-133118	HD 358059	5	0.00	+0.13	-0.56	0.00	+0.24	+0.07	-0.20	+0.18
RAVE J210642.9-682827	UCAC2 2203606	5	+0.53	+0.90	+0.52	+1.32	+0.43		+0.62	+0.83
RAVE J222236.0-013827	BPS CS 29502-092	6	+1.06	-0.33	-1.36	<- 0.11	+1.35		-1.23	

#### Note.

References. Literature citations are as follows: (1) Hill et al. (2002), (2) Hansen et al. (2015), (3) Sakari et al. (2018b), (4) Sakari et al. (2018a), (5) Hansen et al. (2018), and (6) Roederer et al. (2014). Average Uncertainties for [X/Fe] measurements are as follows: Hill et al. (2002):  $\sim$ 0.05-0.20 dex; Hansen et al. (2015):  $\sim$ 0.2-0.3 dex; Sakari et al. (2018a):  $\sim$ 0.05-0.2 dex; Sakari et al. (2018b):  $\sim$ 0.1-0.2 dex; Hansen et al. (2018):  $\sim$ 0.3-0.4 dex; and Roederer et al. (2014):  $\sim$ 0.2-0.3 dex.

(This table is available in machine-readable form.)

<sup>&</sup>lt;sup>a</sup> The [C/Fe] value reported is "as measured," not corrected for evolutionary effects, as in the rest of the paper.

**Table 4**Stellar Atmospheric Parameters for the Program Stars

Name	$T_{\rm eff}$ (K)	log g(cgs)	[Fe/H]	$v_{\rm turb}~({\rm km~s}^{-1})$
RAVE J012931.1-160046	4959	1.70	-2.77	2.65
RAVE J030639.1-692040	4770	1.55	-2.81	1.75
RAVE J035550.9-721151	4990	2.05	-2.64	1.95
RAVE J040618.2-030525	5260	2.75	-1.34	1.80
RAVE J044208.2-342114	4837	1.40	-2.17	2.25
RAVE J045322.6-221040	6115	3.90	-2.54	1.60
RAVE J053817.0-751621	4900	1.65	-2.03	2.20
RAVE J061950.0-531212	5170	2.80	-2.15	1.90
RAVE J071234.0-481405	4612	0.80	-2.92	2.90
RAVE J074824.3–483141	5445	2.00	-2.01	2.25
RAVE J100709.2–180947	4806	1.70	-2.01	1.70
RAVE J111711.0-310951	6070	3.55	-1.90	1.60
RAVE J111912.3–160947	5346	2.25	-1.97	2.00
RAVE J113508.3–111328	6115	4.25	-1.21	1.50
RAVE J113308.5-111328 RAVE J114444.8-112817	5125	2.45	-2.51	1.55
RAVE J115941.7–382043	5287	3.35	-2.51 $-0.94$	1.25
	4860	1.45	-0.94 $-2.34$	2.00
RAVE J123550.1—313111				
RAVE J124154.7-085701	6061	3.65	-2.38	2.80
RAVE J124753.3-390802	4423	1.05	-2.19	2.45
RAVE J130524.5-393126	5008	2.20	-2.11	1.70
RAVE J132141.8-432006	4954	1.25	-2.03	2.35
RAVE J132414.3—180620	4837	1.55	-2.52	2.30
RAVE J134319.3-235814	4896	1.75	-2.64	2.50
RAVE J151558.3-203821	4743	1.10	-2.65	2.30
RAVE J151608.7-212160	4360	0.60	-2.43	2.75
RAVE J153539.5-173455	4882	1.60	-2.58	2.25
RAVE J153830.9-180424	4995	2.00	-2.02	1.85
RAVE J154230.9-210731	4675	0.85	-2.18	2.30
RAVE J155829.6—122434	5067	1.40	-2.58	2.20
RAVE J160245.0-152102	5215	3.00	-1.90	1.50
RAVE J165300.5-005507	4702	1.30	-1.56	2.15
RAVE J171633.4-700902	4608	1.00	-2.65	2.85
RAVE J175159.8-475131	4716	1.65	-1.90	2.00
RAVE J180242.3-440443	4711	1.30	-1.84	2.30
RAVE J183108.2-491105	4545	1.15	-2.09	2.10
RAVE J183623.2-642812	5071	2.20	-2.50	2.35
RAVE J191755.9-544015	4887	1.50	-2.59	2.05
RAVE J192632.8-584657	4590	1.00	-2.49	2.95
RAVE J192819.9-633935	4927	1.70	-2.23	1.85
RAVE J194550.6-392631	4855	1.50	-2.79	1.90
RAVE J201446.1-563530	5044	2.05	-1.75	1.75
RAVE J203706.4-122125	4540	1.05	-2.63	2.90
RAVE J204450.7-371400	4558	0.90	-2.84	3.30
RAVE J204954.4-480045	5206	2.70	-1.79	1.65
RAVE J205149.7-615801	5310	3.15	-1.92	1.55
RAVE J205609.1-133118	4918	1.65	-2.24	1.95
RAVE J210642.9-682827	5026	2.00	-2.92	1.55
RAVE J211413.5-572636	4828	1.30	-2.61	2.65
RAVE J215118.3-135937	5017	2.10	-1.94	1.50
RAVE J222236.0-013827	5202	2.40	-2.87	2.25

(This table is available in machine-readable form.)

(Hansen et al. 2018; Sakari et al. 2018a; Ezzeddine et al. 2020), whose combined 374 stars contain 43% *r*-I and 7% *r*-II stars.

#### 6. Kinematics

Kinematics for our program stars were computed using the galpy Galactic dynamics library (Bovy 2015). We adopt  $R_{\odot} = 8$  kpc as the distance to the Galactic center,  $v_{\rm LSR} = 220$  km s<sup>-1</sup> as the local standard of rest (LSR) velocity (Kerr & Lynden-Bell 1986), and  $(U, V, W)_{\odot} = (-9, 12, 7)$  km s<sup>-1</sup> as the motion of the Sun with respect to the LSR (Mihalas & Binney 1981). Orbital

parameters were derived with the potential code employed by Chiba & Beers (2000), which utilizes the Stäckel potential described in Sommer-Larsen & Zhen (1990). Uncertainties in the orbital parameters were derived through a Markov Chain Monte Carlo (MCMC) sampling method.

To better represent where our sample stars lie in the Lindblad diagram with respect to various Galactic populations, Figure 9 overplots our stars with a reference sample from SDSS (S. Dietz et al. 2020, in preparation). The red filled dots indicate our program stars. The dashed line marks

 Table 5

 Classification Abundances for the Program Stars

				s for the Program Su			
Name	Class	$A(C)_{corr}$	[C/Fe]	[C/Fe] <sub>corr</sub>	[Sr/Fe]	[Ba/Fe]	[Eu/Fe]
RAVE J012931.1-160046	r-II	6.35	$+0.44 \pm 0.25$	$+0.69 \pm 0.25$	$+0.96 \pm 0.30$	$+1.20 \pm 0.30$	$+1.80 \pm 0.30$
RAVE J030639.1-692040		6.08	$+0.08 \pm 0.25$	$+0.46 \pm 0.25$	$-0.53 \pm 0.30$	$-0.31 \pm 0.20$	<+0.35
RAVE J035550.9-721151	r-I	6.11	$+0.32 \pm 0.25$	$+0.32 \pm 0.25$	$+0.53 \pm 0.20$	$-0.08 \pm 0.2$	$+0.60 \pm 0.20$
RAVE J040618.2-030525	$r$ - $\Pi$	7.66	$+0.54 \pm 0.25$	$+0.57 \pm 0.25$		$+0.98 \pm 0.30$	$+1.17 \pm 0.20$
RAVE J044208.2-342114	CEMP-i	7.84	$+1.44 \pm 0.25$	$+1.58 \pm 0.25$		$+0.49 \pm 0.30$	$+0.39 \pm 0.2$
RAVE J045322.6-221040		< 6.19	< 0.00	<+0.30	$-0.29 \pm 0.10$	$-0.73 \pm 0.10$	
RAVE J053817.0-751621		6.91	$+0.18 \pm 0.25$	$+0.51 \pm 0.25$	$-0.63 \pm 0.30$	$-0.24 \pm 0.20$	$+0.44 \pm 0.20$
RAVE J061950.0-531212		6.62	$+0.33 \pm 0.25$	$+0.34 \pm 0.20$	$+1.24 \pm 0.20$	$-0.24 \pm 0.20$	$+0.51 \pm 0.20$
RAVE J071234.0-481405		5.92	$-0.36 \pm 0.25$	$+0.41 \pm 0.25$	$-1.73 \pm 0.30$	$-1.60 \pm 0.20$	< 0.00
RAVE J074824.3-483141	r-I	6.48	$+0.00 \pm 0.25$	$+0.06 \pm 0.25$	$+0.66 \pm 0.20$	$-0.20 \pm 0.30$	$+0.45\pm0.20$
RAVE J100709.2-180947	r-I	6.83	$+0.10 \pm 0.25$	$+0.41 \pm 0.30$	$+1.01 \pm 0.20$		$+0.62 \pm 0.20$
RAVE J111711.0-310951	CEMP-no	7.23	$+0.70 \pm 0.25$	$+0.70 \pm 0.25$	$+1.10 \pm 0.30$	$-0.05 \pm 0.20$	< 0.00
RAVE J111912.3-160947	CEMP-s	7.71	$+1.23 \pm 0.25$	$+1.25 \pm 0.25$	$+0.98 \pm 0.20$	$+1.52 \pm 0.20$	$+0.75 \pm 0.20$
RAVE J113508.3-111328		7.32	$+0.01 \pm 0.25$	$+0.10 \pm 0.25$	$+0.31 \pm 0.20$	$+0.36 \pm 0.30$	< 0.00
RAVE J114444.8-112817	r-I	6.01	$+0.08 \pm 0.25$	$+0.09 \pm 0.25$	$+0.19 \pm 0.20$	$-0.05 \pm 0.20$	$+0.42 \pm 0.20$
RAVE J115941.7-382043	r-I	7.67	$+0.18 \pm 0.25$	$+0.18 \pm 0.25$		$-0.01 \pm 0.20$	$+0.70 \pm 0.20$
RAVE J123550.1-313111	CEMP-r	7.06	$+0.61 \pm 0.25$	$+0.97 \pm 0.25$		$+0.27\pm0.20$	$+0.59 \pm 0.20$
RAVE J124154.7-085701	CEMP-no	6.88	$+0.83 \pm 0.25$	$+0.83 \pm 0.30$	$+0.47 \pm 0.50$	$-0.38 \pm 0.20$	
RAVE J124753.3-390802		6.72	$-0.18 \pm 0.25$	$+0.48 \pm 0.25$		$+0.07 \pm 0.30$	
RAVE J130524.5-393126	r-I	6.50	$+0.17 \pm 0.25$	$+0.18 \pm 0.25$	$+0.43 \pm 0.30$	$+0.12 \pm 0.30$	$+0.76 \pm 0.30$
RAVE J132141.8-432006	r-I	6.74	$-0.23 \pm 0.25$	$+0.34 \pm 0.25$	$+0.67 \pm 0.30$	$+0.04 \pm 0.20$	$+0.66 \pm 0.20$
RAVE J132414.3-180620		6.54	$+0.23 \pm 0.25$	$+0.63 \pm 0.25$	$+0.02 \pm 0.20$	$-0.56 \pm 0.20$	< - 0.04
RAVE J134319.3-235814		6.30	$+0.32 \pm 0.25$	$+0.51 \pm 0.25$	$+0.39 \pm 0.30$	$-0.75 \pm 0.20$	< 0.00
RAVE J151558.3-203821	<i>r</i> -I	6.32	$-0.15 \pm 0.25$	$+0.54 \pm 0.25$	$+0.27 \pm 0.20$	$-0.39 \pm 0.20$	$+0.36 \pm 0.20$
RAVE J151608.7-212160	CEMP-no	7.18	$+0.76 \pm 0.25$	$+1.18 \pm 0.25$		$-0.50 \pm 0.20$	$+0.09 \pm 0.20$
RAVE J153539.5-173455	CEMP-no	6.66	$+0.48 \pm 0.25$	$+0.81 \pm 0.25$	$+0.55 \pm 0.30$	$+0.20 \pm 0.20$	< 0.00
RAVE J153830.9-180424	r-II	6.59	$+0.12 \pm 0.25$	$+0.18 \pm 0.25$	$+0.50 \pm 0.30$	$+0.72\pm0.20$	$+1.52 \pm 0.20$
RAVE J154230.9-210731		6.68	$-0.48 \pm 0.25$	$+0.43 \pm 0.25$	$-1.11 \pm 0.20$	$-1.50 \pm 0.20$	
RAVE J155829.6-122434	r-I	6.39	$+0.00 \pm 0.25$	$+0.54 \pm 0.25$	$+0.65 \pm 0.20$	$+0.23\pm0.20$	$+0.72 \pm 0.20$
RAVE J160245.0-152102	r-I	7.07	$+0.14 \pm 0.25$	$+0.54 \pm 0.25$	$+0.11 \pm 0.20$	$+0.00 \pm 0.20$	$+0.53 \pm 0.20$
RAVE J165300.5-005507	r-I	7.00	$-0.36 \pm 0.25$	$+0.13 \pm 0.25$	$-0.39 \pm 0.30$	$-0.43 \pm 0.20$	$+0.68 \pm 0.20$
RAVE J171633.4-700902	CEMP-r	6.51	$+0.03 \pm 0.25$	$+0.73 \pm 0.25$		$+0.00 \pm 0.30$	$+1.09 \pm 0.30$
RAVE J175159.8-475131	r-I	6.64	$-0.27 \pm 0.25$	$+0.11 \pm 0.25$	$+0.38 \pm 0.30$	$-0.14 \pm 0.30$	$+0.68 \pm 0.20$
RAVE J180242.3-440443	CEMP-r	7.37	$+0.48 \pm 0.25$	$+0.78 \pm 0.25$	$+0.15 \pm 0.30$	$+0.03 \pm 0.30$	$+1.20 \pm 0.30$
RAVE J183108.2-491105		6.65	$-0.32 \pm 0.25$	$+0.31 \pm 0.25$		$-0.05 \pm 0.30$	$+0.32 \pm 0.20$
RAVE J183623.2-642812	r-I	6.41	$+0.47 \pm 0.25$	$+0.48 \pm 0.25$	$+0.66 \pm 0.30$	$+0.09 \pm 0.20$	$+0.72 \pm 0.30$
RAVE J191755.9-544015	CEMP-no	6.69	$+0.44 \pm 0.25$	$+0.85 \pm 0.25$	$+0.47 \pm 0.30$	$-0.42 \pm 0.20$	<+0.17
RAVE J192632.8-584657	<i>r</i> -I	6.45	$-0.22 \pm 0.25$	$+0.51 \pm 0.25$	$+0.38 \pm 0.30$	$-0.35 \pm 0.20$	$+0.76 \pm 0.20$
RAVE J192819.9–633935	r-I	6.69	$+0.17 \pm 0.25$	$+0.49 \pm 0.25$		$+0.09 \pm 0.20$	$+0.45 \pm 0.30$
RAVE J194550.6-392631	r-I	6.23	$+0.17 \pm 0.25$	$+0.59 \pm 0.25$	$+0.20 \pm 0.30$	$+0.40 \pm 0.20$	$+0.90 \pm 0.20$
RAVE J201446.1-563530	CEMP-i	8.10	$+1.37 \pm 0.25$	$+1.42 \pm 0.25$		$+0.85 \pm 0.30$	$+0.78 \pm 0.30$
RAVE J203706.4–122125	CEMP-no	6.83	$+0.70 \pm 0.25$	$+1.30 \pm 0.25$	$-0.13 \pm 0.30$	$+0.00 \pm 0.20$	$+0.20 \pm 0.30$
RAVE J204450.7-371400	CEMP-no	6.61	$+0.37 \pm 0.25$	$+1.02 \pm 0.25$	$+0.63 \pm 0.30$	$-0.69 \pm 0.30$	<+0.10
RAVE J204954.4-480045		6.90	$+0.24 \pm 0.25$	$+0.26 \pm 0.25$	$+0.52 \pm 0.20$	$+0.11 \pm 0.20$	$+0.18 \pm 0.20$
RAVE J205149.7-615801	 <i>r</i> -I	6.74	$+0.24 \pm 0.25$ $+0.22 \pm 0.25$	$+0.23 \pm 0.25$ $+0.23 \pm 0.25$	$+0.02 \pm 0.20$ $+0.00 \pm 0.30$	$-0.25 \pm 0.20$	$+0.60 \pm 0.20$
RAVE J205609.1–133118		6.80	$+0.22 \pm 0.25$ $+0.24 \pm 0.25$	$+0.23 \pm 0.25$ $+0.61 \pm 0.25$	$+0.00 \pm 0.30$ $+0.07 \pm 0.20$	$-0.20 \pm 0.20$ $-0.20 \pm 0.20$	$+0.00 \pm 0.20$ $+0.18 \pm 0.20$
RAVE J203009.1-133118 RAVE J210642.9-682827		5.98	$+0.24 \pm 0.25$ $+0.43 \pm 0.25$	$+0.47 \pm 0.25$		$-0.20 \pm 0.20$ $+0.62 \pm 0.20$	$0.83 \pm 0.30$
RAVE J210042.9-082827 RAVE J211413.5-572636	 CEMP-no	6.76	$+0.43 \pm 0.25$ $+0.43 \pm 0.25$	$+0.47 \pm 0.25$ $+0.94 \pm 0.25$		$-0.02 \pm 0.20$ $-1.13 \pm 0.20$	< 0.00
RAVE J211413.3-372030 RAVE J215118.3-135937	<i>r</i> -I	6.85	$+0.43 \pm 0.25$ $+0.34 \pm 0.25$	$+0.34 \pm 0.25$ $+0.36 \pm 0.25$	$+0.56 \pm 0.30$	$-0.85 \pm 0.20$	$+0.37 \pm 0.30$
RAVE J213116.5-133937 RAVE J222236.0-013827	CEMP-no	6.92	$+0.34 \pm 0.25$ $+1.35 \pm 0.25$	$+0.36 \pm 0.25$ $+1.36 \pm 0.25$		$-0.83 \pm 0.30$ $-1.23 \pm 0.20$	
KA VE J222230.U=01302/	CEMIT-110	0.94	$\pm 1.55 \pm 0.25$	$\pm 1.50 \pm 0.23$	•••	$-1.23 \pm 0.20$	•••

(This table is available in machine-readable form.)

the  $L_{\rm z}=0$  line, separating prograde and retrograde populations. The green, blue, and red ellipses indicate approximate locations of important reference populations. Green indicates the strongly bound, prograde disk system. Blue indicates the "plume" that marks the remnant of the large inner-halo progenitor referred to as Gaia Enceladus (Helmi et al. 2018) or the Gaia Sausage (Belokurov et al. 2018; Myeong et al. 2018). Red indicates high-energy, retrograde stars in the outer halo. The stars in our sample, being relatively bright and (presently) close-by, are largely more strongly bound, and

comprise members of the disk system and inner-halo population. No high-energy outer-halo stars are found in our sample, although the more energetic stars have higher uncertainties on their orbital-value determinations, so their membership is somewhat uncertain.

# 7. Comparison with s- and i-process Models and Origin Scenarios

Finally, we compare our results with chemical-abundance models in order to investigate the <sup>13</sup>C-pocket efficiencies

**Table 6**Abundance Ratios for the Elements Mg, Ca, Sc II, Ti I, and Ti II

Name	[Mg/Fe]	[Ca/Fe]	[Sc II/Fe]	[Ti I/Fe]	[Ti II/Fe]
RAVE J012931.1-160046	$+0.47 \pm 0.19$	$+0.47 \pm 0.15$	$+0.03 \pm 0.01$	$+0.31 \pm 0.18$	$+0.33 \pm 0.12$
RAVE J030639.1-692040	$+0.32 \pm 0.10$		$-0.10 \pm 0.10$	$+0.14 \pm 0.10$	$+0.12\pm0.08$
RAVE J035550.9-721151	$+0.46 \pm 0.10$	$+0.42\pm0.14$	$+0.11 \pm 0.03$	$+0.22\pm0.07$	$+0.37 \pm 0.11$
RAVE J040618.2-030525		$+0.41\pm0.05$	$+0.47 \pm 0.10$	$+0.23 \pm 0.10$	$+0.27\pm0.15$
RAVE J044208.2-342114		$+0.48\pm0.04$	$+0.24 \pm 0.10$	$+0.26 \pm 0.11$	$+0.23\pm0.08$
RAVE J045322.6-221040	$+0.27\pm0.04$	$+0.44\pm0.10$	$+0.21 \pm 0.07$	$+0.43 \pm 0.06$	$+0.49\pm0.09$
RAVE J053817.0-751621		$+0.60\pm0.22$	$+0.05\pm0.09$	$+0.24 \pm 0.14$	$+0.31 \pm 0.15$
RAVE J061950.0-531212	$+0.41 \pm 0.03$	$+0.33 \pm 0.11$	$+0.04 \pm 0.05$	$+0.25\pm0.11$	$+0.33 \pm 0.12$
RAVE J071234.0-481405	$+0.48\pm0.14$	$+0.23\pm0.06$	$+0.07 \pm 0.03$	$+0.32 \pm 0.05$	$+0.39 \pm 0.14$
RAVE J074824.3-483141	$+0.32 \pm 0.10$	$+0.38 \pm 0.05$	$+0.08 \pm 0.05$	$+0.26 \pm 0.11$	$+0.32 \pm 0.13$
RAVE J100709.2-180947	$+0.39 \pm 0.10$	$+0.71\pm0.09$	$+0.13 \pm 0.03$	$+0.20 \pm 0.12$	$+0.37 \pm 0.19$
RAVE J111711.0-310951	$+0.24 \pm 0.08$	$+0.37\pm0.07$	$-0.04 \pm 0.01$	$+0.29\pm0.09$	$+0.40\pm0.08$
RAVE J111912.3-160947	$+0.31 \pm 0.13$	$+0.38 \pm 0.12$	$+0.15 \pm 0.09$	$+0.32\pm0.08$	$+0.36 \pm 0.15$
RAVE J113508.3-111328	$+0.31 \pm 0.10$	$+0.38 \pm 0.14$	$+0.17 \pm 0.04$	$+0.23\pm0.07$	$+0.20\pm0.07$
RAVE J114444.8-112817	$+0.42 \pm 0.09$	$+0.42\pm0.08$	$-0.01 \pm 0.04$	$+0.26 \pm 0.09$	$+0.31 \pm 0.11$
RAVE J115941.7-382043		$+0.24 \pm 0.10$	$+0.35\pm0.02$	$+0.35\pm0.07$	$+0.50 \pm 0.13$
RAVE J123550.1-313111	$+0.41 \pm 0.10$	$+0.46 \pm 0.06$	$-0.10 \pm 0.06$	$+0.20 \pm 0.13$	$+0.26 \pm 0.14$
RAVE J124154.7-085701	$+0.45\pm0.12$	$+0.60 \pm 0.10$	$+0.20 \pm 0.01$	$+0.51 \pm 0.06$	$+0.37\pm0.12$
RAVE J124753.3-390802		$+0.22\pm0.10$	$+0.29\pm0.10$	$+0.29 \pm 0.06$	$+0.44 \pm 0.12$
RAVE J130524.5-393126		$+0.43\pm0.06$	$+0.10 \pm 0.04$	$+0.23\pm0.09$	$+0.42 \pm 0.12$
RAVE J132141.8-432006	$+0.30 \pm 0.10$	$+0.27\pm0.01$	$-0.07\pm0.02$	$+0.18 \pm 0.10$	$+0.21\pm0.11$
RAVE J132414.3-180620	$+0.31 \pm 0.08$	$+0.27\pm0.07$	$-0.18 \pm 0.09$	$+0.10 \pm 0.11$	$+0.24 \pm 0.12$
RAVE J134319.3-235814	$+0.40\pm0.10$		$+0.06 \pm 0.01$	$+0.17 \pm 0.11$	$+0.35\pm0.14$
RAVE J151558.3-203821	$+0.52\pm0.09$	$+0.37\pm0.08$	$+0.00 \pm 0.05$	$+0.19 \pm 0.06$	$+0.33 \pm 0.14$
RAVE J151608.7-212160		$+0.54 \pm 0.10$	$+0.07\pm0.04$	$+0.09 \pm 0.06$	$+0.41 \pm 0.16$
RAVE J153539.5-173455	$+0.31 \pm 0.08$	$+0.29 \pm 0.05$	$+0.06 \pm 0.02$	$+0.22 \pm 0.10$	$+0.32 \pm 0.05$
RAVE J153830.9-180424		$+0.35 \pm 0.04$	$+0.09 \pm 0.08$	$+0.19 \pm 0.09$	$+0.30 \pm 0.13$
RAVE J154230.9-210731	$+0.59 \pm 0.09$	$+0.47\pm0.07$	$+0.13 \pm 0.03$	$+0.18 \pm 0.13$	$+0.19 \pm 0.14$
RAVE J155829.6-122434	$+0.47 \pm 0.13$	$+0.37 \pm 0.06$	$+0.02\pm0.02$	$+0.35 \pm 0.07$	$+0.37 \pm 0.13$
RAVE J160245.0-152102	$+0.19 \pm 0.04$	$+0.24 \pm 0.12$	$-0.08 \pm 0.06$	$+0.02 \pm 0.06$	$+0.22 \pm 0.10$
RAVE J165300.5-005507	•••	$+0.39 \pm 0.10$	$+0.10 \pm 0.03$	$+0.17 \pm 0.10$	$+0.42 \pm 0.15$
RAVE J171633.4-700902	•••	$+0.29 \pm 0.06$	$+0.02 \pm 0.07$	$+0.27\pm0.08$	$+0.43 \pm 0.14$
RAVE J175159.8-475131	•••	$+0.32 \pm 0.10$	$+0.19 \pm 0.11$	$+0.30 \pm 0.09$	$+0.37 \pm 0.10$
RAVE J180242.3-440443	•••		$+0.13 \pm 0.11$	$+0.24 \pm 0.12$	$+0.29 \pm 0.19$
RAVE J183108.2-491105		$+0.59 \pm 0.25$	$+0.02 \pm 0.07$	$+0.28 \pm 0.10$	$+0.46 \pm 0.07$
RAVE J183623.2-642812	$+0.40 \pm 0.12$	$+0.41 \pm 0.08$	$+0.07 \pm 0.05$	$+0.27 \pm 0.14$	$+0.46 \pm 0.12$
RAVE J191755.9-544015	$+0.31 \pm 0.13$	$+0.40 \pm 0.13$	$-0.12 \pm 0.02$	$+0.16 \pm 0.08$	$+0.26 \pm 0.15$
RAVE J192632.8-584657	$+0.27 \pm 0.08$	$+0.40 \pm 0.14$	$+0.05 \pm 0.07$	$+0.25\pm0.07$	$+0.36 \pm 0.16$
RAVE J192819.9-633935	$+0.61 \pm 0.10$	$+0.38 \pm 0.07$	$+0.00 \pm 0.03$	$+0.27 \pm 0.09$	$+0.33 \pm 0.11$
RAVE J194550.6-392631	$+0.40 \pm 0.06$	$+0.33 \pm 0.05$	$+0.11 \pm 0.02$	$+0.29 \pm 0.09$	$+0.40 \pm 0.13$
RAVE J201446.1-563530	•••	$+0.39 \pm 0.10$	$+0.37 \pm 0.07$	$+0.50 \pm 0.13$	$+0.57 \pm 0.17$
RAVE J203706.4-122125	$+0.42 \pm 0.05$	$+0.30 \pm 0.13$	$+0.23 \pm 0.12$	$+0.21 \pm 0.04$	$+0.49 \pm 0.15$
RAVE J204450.7-371400	$+0.48 \pm 0.07$	$+0.25\pm0.04$	$+0.04 \pm 0.35$	$+0.24 \pm 0.13$	$+0.35 \pm 0.18$
RAVE J204954.4-480045	$+0.40\pm0.10$	$+0.26 \pm 0.05$	$+0.15 \pm 0.06$	$+0.25 \pm 0.06$	$+0.34 \pm 0.13$
RAVE J205149.7-615801	$+0.36 \pm 0.10$	$+0.30 \pm 0.04$	$+0.01 \pm 0.04$	$+0.23 \pm 0.10$	$+0.37 \pm 0.10$
RAVE J205609.1-133118	$+0.50 \pm 0.03$	$+0.30 \pm 0.08$	$-0.07 \pm 0.03$	$+0.21 \pm 0.11$	$+0.27 \pm 0.11$
RAVE J210642.9-682827	$+0.50 \pm 0.10$	$+0.52 \pm 0.08$	$-0.06 \pm 0.08$	$+0.31 \pm 0.09$	$+0.25 \pm 0.13$
RAVE J211413.5-572636	$+0.37 \pm 0.12$	$+0.25 \pm 0.05$	$-0.08 \pm 0.05$	$+0.20 \pm 0.07$	$+0.28 \pm 0.17$
RAVE J215118.3-135937	$+0.55 \pm 0.10$	$+0.81 \pm 0.09$	$+0.06 \pm 0.10$	$+0.28 \pm 0.06$	$+0.41 \pm 0.10$
RAVE J222236.0-013827	$+0.19 \pm 0.01$	$+0.48 \pm 0.14$	$+0.28 \pm 0.04$	$+0.17 \pm 0.06$	$+0.23 \pm 0.14$

Note. Uncertainties are taken as the standard deviation of multiple measurements; in cases where only one line was measurable, a nominal uncertainty of 0.10 dex has been assigned.

(This table is available in machine-readable form.)

(where the C-pocket refers to the thin layer of radiative carbon burning that occurs in the top layer of the He-shell after the third dredge-up episode of an AGB star) ultimately responsible for our three Ba-rich stars. We also consider the divergence of the chemical displacement scheme to investigate origin scenarios of our program stars, by testing whether they formed from gas enriched by multiple versus single supernovae.

## 7.1. The Ba-rich Stars

Three of our program CEMP stars are highly enriched in Ba, likely due to mass transfer from an AGB companion—one CEMP-*s* star (RAVE J111912.3-160947) and two CEMP-*i* stars (RAVE 044208.2-342114 and RAVE 201446.1-563530). All three are compared with theoretical predictions for a variety of AGB models, varying in mass and <sup>13</sup>C-pocket efficiencies,

Table 7
Abundance Ratios for the Elements V I, Cr I, Cr II, Mn, Co, Ni, and Zn

Name	[V I/Fe]	[Cr I/Fe]	[Cr II/Fe]	[Mn/Fe]	[Co/Fe]	[Ni/Fe]	[Zn/Fe]
RAVE J012931.1-160046		$-0.21 \pm 0.16$		$-0.44 \pm 0.09$	$+0.64 \pm 0.10$	$+0.01 \pm 0.12$	$+0.30 \pm 0.10$
RAVE J030639.1-692040		$-0.32 \pm 0.11$		$-0.47 \pm 0.10$	$-0.09 \pm 0.10$	$+0.14 \pm 0.16$	
RAVE J035550.9-721151	$+0.13 \pm 0.10$	$-0.23 \pm 0.08$	$+0.18\pm0.02$	$-0.41 \pm 0.10$	$+0.48 \pm 0.02$	$+0.11 \pm 0.06$	$+0.26 \pm 0.01$
RAVE J040618.2-030525	$+0.29 \pm 0.10$	$-0.03 \pm 0.14$	$-0.09 \pm 0.10$	$-0.23 \pm 0.03$		$+0.00 \pm 0.08$	$-0.01 \pm 0.13$
RAVE J044208.2-342114		$+0.00 \pm 0.21$		$-0.17 \pm 0.11$		$+0.00 \pm 0.06$	$+0.10 \pm 0.10$
RAVE J045322.6-221040		$-0.17 \pm 0.14$		$-0.44 \pm 0.10$	$+0.17 \pm 0.10$	$+0.25\pm0.10$	
RAVE J053817.0-751621	$+0.06 \pm 0.10$	$-0.11 \pm 0.10$		$-0.35 \pm 0.05$	$-0.12 \pm 0.10$	$+0.05\pm0.11$	$+0.01 \pm 0.03$
RAVE J061950.0-531212		$-0.20 \pm 0.09$		$-0.49 \pm 0.07$	$+0.54 \pm 0.08$	$+0.11 \pm 0.05$	$+0.44 \pm 0.10$
RAVE J071234.0-481405	$-0.13 \pm 0.10$	$-0.20 \pm 0.06$		$-0.59 \pm 0.01$		$+0.04 \pm 0.08$	$+0.13 \pm 0.10$
RAVE J074824.3-483141	$+0.10 \pm 0.10$	$-0.11 \pm 0.06$	$+0.08 \pm 0.01$	$-0.31 \pm 0.07$	$+0.27 \pm 0.09$	$+0.05 \pm 0.07$	$+0.14 \pm 0.13$
RAVE J100709.2-180947	$+0.21 \pm 0.10$	$-0.10 \pm 0.10$	$+0.26 \pm 0.06$	$-0.34 \pm 0.07$		$+0.03 \pm 0.07$	$+0.21 \pm 0.08$
RAVE J111711.0-310951		$-0.21 \pm 0.03$	$-0.19 \pm 0.10$			$+0.07 \pm 0.03$	$+0.30 \pm 0.10$
RAVE J111912.3-160947	$+0.06 \pm 0.10$	$-0.10 \pm 0.07$	$+0.12 \pm 0.05$	$-0.30 \pm 0.10$	$+0.00 \pm 0.10$	$-0.03 \pm 0.14$	$+0.14 \pm 0.09$
RAVE J113508.3-111328	$+0.19 \pm 0.10$	$-0.09 \pm 0.09$	$+0.03 \pm 0.10$	$-0.22 \pm 0.02$		$+0.01 \pm 0.11$	$+0.07 \pm 0.05$
RAVE J114444.8-112817	$+0.01 \pm 0.10$	$-0.18 \pm 0.09$	$+0.17 \pm 0.01$	$-0.44 \pm 0.04$	$+0.25\pm0.01$	$+0.02 \pm 0.07$	$+0.21 \pm 0.03$
RAVE J115941.7-382043		$+0.08 \pm 0.09$	$+0.17 \pm 0.08$	$+0.20 \pm 0.10$		$+0.01 \pm 0.12$	$+0.20 \pm 0.07$
RAVE J123550.1-313111		$-0.32 \pm 0.11$	$+0.08 \pm 0.07$	$-0.34 \pm 0.10$	•••	$+0.00 \pm 0.13$	$+0.06 \pm 0.05$
RAVE J124154.7-085701		$-0.13 \pm 0.03$	$+0.33 \pm 0.10$	$-0.13 \pm 0.10$		$+0.13 \pm 0.05$	$+0.37 \pm 0.10$
RAVE J124753.3-390802		$-0.12 \pm 0.13$		$-0.31 \pm 0.09$		$-0.05 \pm 0.12$	$+0.23 \pm 0.02$
RAVE J130524.5-393126	$-0.20 \pm 0.10$	$-0.19 \pm 0.10$	•••	$-0.60 \pm 0.09$	•••	$-0.01 \pm 0.11$	
RAVE J132141.8-432006	$-0.13 \pm 0.10$	$-0.17 \pm 0.06$	$+0.15 \pm 0.07$	$-0.36 \pm 0.02$	•••	$+0.00 \pm 0.09$	$+0.14 \pm 0.08$
RAVE J132414.3-180620	$-0.23 \pm 0.10$	$-0.24 \pm 0.05$	$-0.06 \pm 0.10$	$-0.49 \pm 0.05$		$-0.04 \pm 0.05$	$+0.13 \pm 0.03$
RAVE J134319.3-235814		$-0.25 \pm 0.04$	$+0.12 \pm 0.10$	$-0.41 \pm 0.04$	$+0.33 \pm 0.01$	$+0.06 \pm 0.08$	$+0.12 \pm 0.10$
RAVE J151558.3-203821	$-0.26 \pm 0.10$	$-0.23 \pm 0.04$	$+0.08 \pm 0.08$	$-0.40 \pm 0.03$	$+0.19 \pm 0.10$	$+0.00 \pm 0.08$	$+0.17 \pm 0.10$
RAVE J151608.7-212160		$-0.33 \pm 0.06$	$+0.20 \pm 0.01$	$-0.46 \pm 0.07$		$-0.04 \pm 0.08$	$+0.32 \pm 0.05$
RAVE J153539.5-173455	$-0.10 \pm 0.10$	$-0.20 \pm 0.14$		$-0.32 \pm 0.05$		$+0.09 \pm 0.10$	$+0.34 \pm 0.08$
RAVE J153830.9-180424	$-0.02 \pm 0.10$	$-0.13 \pm 0.10$	$+0.08 \pm 0.04$	$-0.26 \pm 0.32$	$+0.75 \pm 0.08$	$+0.00 \pm 0.06$	$+0.06 \pm 0.08$
RAVE J154230.9-210731	$+0.15 \pm 0.10$	$-0.40 \pm 0.08$		$-0.23 \pm 0.10$	$+0.41 \pm 0.04$	$+0.09 \pm 0.07$	$+0.14 \pm 0.10$
RAVE J155829.6-122434	$-0.05 \pm 0.10$	$-0.25 \pm 0.12$	$+0.16 \pm 0.10$	$-0.45 \pm 0.05$	$+0.35 \pm 0.07$	$+0.08 \pm 0.06$	$+0.33 \pm 0.01$
RAVE J160245.0-152102	$+0.03 \pm 0.10$	$-0.32 \pm 0.08$	$+0.05 \pm 0.04$	$-0.56 \pm 0.02$	$+0.04 \pm 0.08$	$-0.14 \pm 0.03$	$+0.02 \pm 0.05$
RAVE J165300.5-005507		$-0.15 \pm 0.10$	$+0.03 \pm 0.10$			$-0.04 \pm 0.05$	$+0.11 \pm 0.03$
RAVE J171633.4-700902	$+0.28 \pm 0.10$	$-0.08 \pm 0.08$	$+0.09 \pm 0.10$	$-0.14 \pm 0.01$	•••	$+0.20 \pm 0.10$	$+0.37 \pm 0.04$
RAVE J175159.8-475131		$-0.09 \pm 0.14$	$+0.04 \pm 0.10$	$-0.22 \pm 0.03$		$-0.07 \pm 0.09$	$+0.12 \pm 0.12$
RAVE J180242.3-440443		$-0.04 \pm 0.03$	$-0.02 \pm 0.10$	$-0.21 \pm 0.10$		$-0.06 \pm 0.08$	$+0.09 \pm 0.12$
RAVE J183108.2-491105	$+0.20 \pm 0.10$	$-0.03 \pm 0.08$	$-0.04 \pm 0.10$	$-0.19 \pm 0.05$	$-0.07 \pm 0.10$	$+0.00 \pm 0.07$	$+0.02 \pm 0.07$
RAVE J183623.2-642812		$-0.20 \pm 0.12$		$-0.36 \pm 0.04$		$-0.03 \pm 0.12$	$+0.19 \pm 0.10$
RAVE J191755.9-544015	•••	$-0.21 \pm 0.08$	$+0.14 \pm 0.04$	$-0.37 \pm 0.05$	$+0.41 \pm 0.10$	$+0.09 \pm 0.08$	$+0.17 \pm 0.02$
RAVE J192632.8-584657	$-0.06 \pm 0.10$	$-0.18 \pm 0.10$	$-0.17 \pm 0.10$	$-0.43 \pm 0.02$		$+0.08 \pm 0.08$	
RAVE J192819.9-633935	$+0.10 \pm 0.10$	$-0.19 \pm 0.05$	$+0.13 \pm 0.03$	$-0.46 \pm 0.02$	$-0.07 \pm 0.10$	$-0.01 \pm 0.10$	$+0.10 \pm 0.10$
RAVE J194550.6-392631	$+0.03 \pm 0.10$	$-0.25 \pm 0.08$		$-0.54 \pm 0.10$	$+0.37 \pm 0.10$	$-0.01 \pm 0.02$	$+0.12 \pm 0.02$
RAVE J201446.1–563530	$+0.08 \pm 0.10$	$-0.06 \pm 0.08$		$-0.39 \pm 0.10$		$-0.03 \pm 0.04$	$-0.06 \pm 0.10$
RAVE J203706.4-122125	$-0.12 \pm 0.10$	$-0.18 \pm 0.04$		$-0.31 \pm 0.10$		$+0.03 \pm 0.09$	$+0.19 \pm 0.10$
RAVE J204450.7-371400	$-0.07 \pm 0.10$	$-0.13 \pm 0.02$	$+0.02 \pm 0.02$	$-0.32 \pm 0.07$	•••	$+0.14 \pm 0.14$	$+0.34 \pm 0.06$
RAVE J204954.4-480045	$+0.46 \pm 0.10$	$-0.13 \pm 0.02$ $-0.13 \pm 0.06$	$+0.02 \pm 0.02$ $+0.11 \pm 0.09$	$-0.36 \pm 0.02$	$+0.33 \pm 0.22$	$-0.09 \pm 0.10$	$+0.00 \pm 0.02$
RAVE J205149.7-615801	$-0.09 \pm 0.10$	$-0.12 \pm 0.06$	$+0.23 \pm 0.03$	$-0.27 \pm 0.03$	$+0.08 \pm 0.10$	$+0.06 \pm 0.06$	$+0.20 \pm 0.01$
RAVE J205609.1–133118	$-0.05 \pm 0.10$ $-0.15 \pm 0.10$	$-0.12 \pm 0.00$ $-0.20 \pm 0.04$	$+0.23 \pm 0.03$ $+0.07 \pm 0.03$	$-0.53 \pm 0.04$	$+0.33 \pm 0.10$ $+0.33 \pm 0.11$	$-0.03 \pm 0.07$	$+0.20 \pm 0.01$ $+0.05 \pm 0.03$
RAVE J203009.1-133118 RAVE J210642.9-682827	$-0.13 \pm 0.10$ $-0.27 \pm 0.10$	$-0.20 \pm 0.04$ $-0.22 \pm 0.13$	+0.07 ± 0.03	$-0.43 \pm 0.04$ $-0.43 \pm 0.12$	+0.33 ± 0.11	$-0.03 \pm 0.07$ $+0.15 \pm 0.10$	$+0.03 \pm 0.03$ $+0.24 \pm 0.08$
RAVE J211413.5-572636	-0.27 ± 0.10 	$-0.25 \pm 0.13$ $-0.25 \pm 0.10$	$+0.12 \pm 0.08$	$-0.43 \pm 0.12$ $-0.27 \pm 0.01$		$+0.13 \pm 0.10$ $+0.13 \pm 0.06$	$+0.24 \pm 0.03$ $+0.25 \pm 0.01$
RAVE J211413.3-372030 RAVE J215118.3-135937		$-0.23 \pm 0.10$ $-0.11 \pm 0.03$	+0.12 ± 0.08 	$-0.27 \pm 0.01$ $-0.40 \pm 0.09$	$+0.29 \pm 0.10$	$+0.13 \pm 0.00$ $+0.00 \pm 0.10$	$-0.16 \pm 0.10$
RAVE J222236.0-013827		$-0.11 \pm 0.03$ $-0.21 \pm 0.12$		$-0.12 \pm 0.11$	$+0.67 \pm 0.10$	$+0.00 \pm 0.10$ $+0.12 \pm 0.08$	$+0.50 \pm 0.10$
10.1 V L 3222230.0-013627	•••	$-0.21 \pm 0.12$		$-0.12 \pm 0.11$	$\pm 0.07 \pm 0.10$	⊤0.12 ± 0.00	$\pm 0.50 \pm 0.10$

Note. Uncertainties are taken as the standard deviation of multiple measurements; in cases where only one line was measurable, a nominal uncertainty of 0.10 dex has been assigned.

(This table is available in machine-readable form.)

taken from Bisterzo et al. (2010). We find that a model of  $1.3\,M_\odot$  with standard pocket efficiency fits our CEMP-i stars well, but that a lower efficiency may be required to fit the abundances of the CEMP-s star. The results are shown in the left panel of Figure 10. Similar tests for a larger sample of CEMP stars from our full  $\sim$ 200 star sample will be considered once their analysis is completed.

## 7.2. Origin Scenarios

We consider the origin scenarios for our program stars, contrasting the cases of enrichment by a single (monoenriched) supernova with that from several supernovae (multienriched), using the divergence of the chemical displacement approach described by Hartwig et al. (2018), and shown in the right panel of Figure 10. Broadly, stars that are monoenriched are expected to

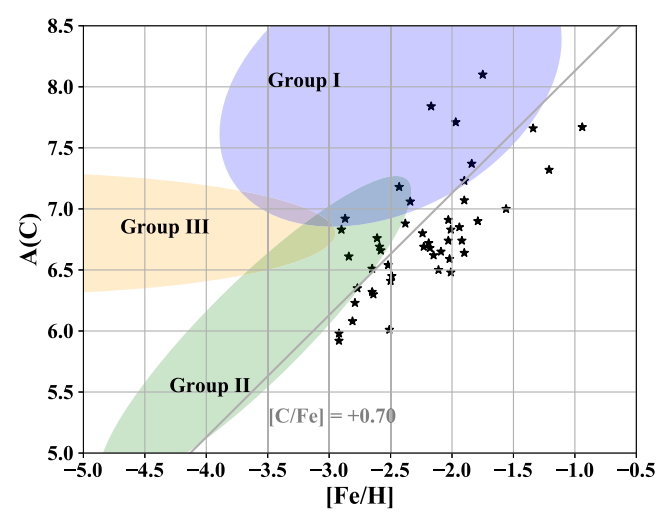


**Figure 8.** Location of our program stars in the A(C)–[Fe/H] space with overlaid groupings, following Yoon et al. (2016). Five of the 15 CEMP stars clearly lie in Group I, seven in Group II, three in the Group I/II overlap region, and none in Group III. The rest of our sample lies below the adopted cutoff for CEMP stars, [C/Fe] = +0.70, shown as a gray line.

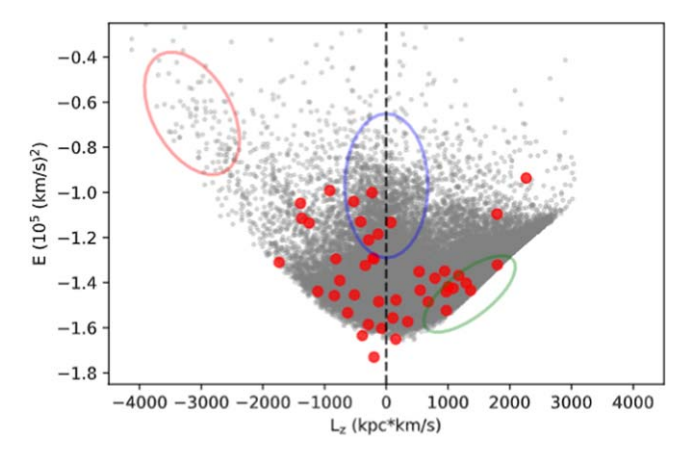


**Figure 9.** Stars in our sample (red filled circles) plotted in Energy- $L_{\rm Z}$  space on top of a reference sample of SDSS stars (gray dots) from S. Dietz et al. (2020, in preparation). The dashed line marks the  $L_{\rm z}=0$  line, separating prograde and retrograde populations. The green ellipse indicates the strongly bound, prograde disk population, blue indicates the "plume" that marks the remnant of the large inner-halo progenitor referred to as Gaia–Enceladus (Helmi et al. 2018) or the Gaia–Sausage (Belokurov et al. 2018; Myeong et al. 2018), and pink indicates high-energy, retrograde stars in the outer halo.

occupy a larger region in the [Mg/C] versus [Fe/H] abundance space. For stars that form from gas enriched by multiple supernovae, this region shrinks, since the abundances of such stars are effectively weighted averages of mono-enriched stars, resulting in a more centrally concentrated space. This change in the occupation of abundance space can be expressed by a vector field of chemical displacement, and its divergence quantifies regions of mono- and multienrichment. The contours illustrate a positive divergence (from 0 to 160 in steps of 40; compare with Figure 14 in Hartwig et al. 2018), and highlight regions of the abundance space where we expect stars to be mono- versus multienriched.

Only two out of nine newly discovered CEMP stars for which Mg abundances are available exhibit a mild tendency for multienrichment (the region to the right of the purple contour in Figure 10, right panel). Their location on the diagram is driven by their relatively high [Fe/H] ( $[Fe/H] \sim -1.9$ ). One is a

strongly bound CEMP-no star on a retrograde orbit (J111711.0 -310951), and one is a CEMP-s star (J111912.3-160947) that lies very close to the inner-halo population in the Energy- $L_z$  space shown in Figure 9. The other stars, which are more metal-poor (down to  $[{\rm Fe/H}] \sim -2.9$ ), follow along the blue contour indicating monoenrichment; they do not preferentially occupy any particular location in Figure 9. This implies that the majority of the CEMP stars in our sample are likely to have formed from gas enriched by only one progenitor supernova, rather than by many. These results are consistent with expectations based on yields from faint supernovae by Nomoto et al. (2013) and Ishigaki et al. (2014).

#### 8. Summary and Outlook

We present a limited set of chemical-abundance measurements and kinematics for a new sample of 50 metal-poor (MP; [Fe/H] < -1.0) and very metal-poor (VMP; [Fe/H] < -2.0) stars in the metallicity range -2.92 < [Fe/H] < -0.94, based on high-resolution ( $R \sim 40,000$  spectroscopic data collected with the HRS on the Southern African Large Telescope. Subclassifications of our program stars indicate that 15 (30%) of these are CEMP stars, nine of these are CEMP-no stars (eight of which are newly discovered), one is a CEMP-s star, and two are likely CEMP-i stars. Twenty-six of our program stars (52%) are r-process-enhanced stars (21 r-I, and newly discovered, and 5 r-II stars, two of which are newly discovered members of the sparsely populated CEMP-r subclass.

We also find that there are eight stars in our sample that, on the basis of their abundances and kinematics, are possible members of the metal-weak thick disk. Further chemical-abundance analysis at higher resolution over an expanded wavelength range would prove useful in the study of the differing enrichment mechanisms, which are responsible for the differences in the chemical-evolution histories of the halo and the thick disk.

We compare our stellar parameters with those obtained by RAVE DR4, RAVE DR5, and Placco et al. (2018), and find moderate to good agreement for most stars. We argue that a number of the stars with [Fe/H] and [C/Fe] estimates from SALT disagree with those reported by Placco et al. (2018), most likely due to their cooler temperatures and relatively strong molecular carbon bands. Application of a new procedure to the medium-resolution spectra for these stars, described by Yoon et al. (2020), results in improved agreement with our high-resolution SALT determinations. Comparison with previous stellar atmospheric parameters and a limited set of chemical abundances with previous high-resolution analyses for nine stars indicate reasonably good agreement.

We also compare our results with chemical-enrichment models to investigate the <sup>13</sup>C-pocket efficiencies of AGB stars that are likely responsible for production of the heavy elements for our three Ba-rich stars, and show that most of our program stars are consistent with mono-, rather than multienrichment, scenarios.

Additional higher S/N high-resolution spectra for the four stars in this sample belonging to poorly populated subclasses (two CEMP-*r*II stars and two CEMP-*i* stars), from which a larger number of neutron-capture elements can be obtained, would be especially valuable. Analysis of the remaining ~150 stars from our SALT program, now underway (J. Zepeda et al. 2020, in preparation) will improve our estimates of the frequencies of the various subclasses found in the present sample, and identify additional astrophysically interesting stars.

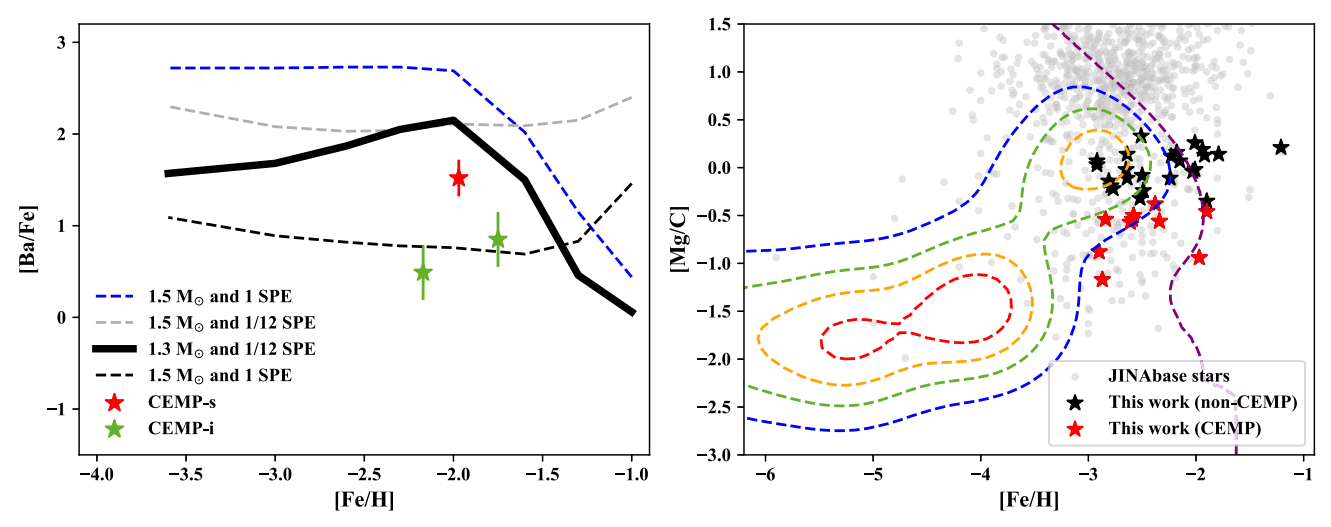


Figure 10. (Left panel) The three Ba-rich stars in our sample (the CEMP-s star RAVE J111912.3-160947, and the CEMP-i stars RAVE J044208.2-342114 and RAVE J201446.1-563530), are plotted in the [Ba/Fe]-[Fe/H] space, along with theoretical yield predictions for two AGB stars with different initial masses and  $^{13}$ C-pocket efficiencies, where the C-pocket refers to the thin layer of radiative carbon burning that occurs in the top layer of the He shell after the third dredge-up episode of an AGB star. The dashed gray and blue lines represent models with 1.5  $M_{\odot}$  and 1/12 and 1 standard pocket efficiency (SPE), respectively. The solid black and dashed black lines represent models with 1.3  $M_{\odot}$  and 1/12 SPE and 1 SPE, respectively. Data were taken from Tables B5 and B6 of Bisterzo et al. (2010). We find that our CEMP-i stars fall along the 1.3  $M_{\odot}$  SPE track, while the CEMP-s star falls between the 1.3  $M_{\odot}$  1/12 SPE and 1 SPE track. (Right panel) Comparison of our newly identified stars with available C and Mg abundances to a diagnostic for monoenrichment or multienrichment proposed by Hartwig et al. (2018). The contours illustrate the likelihood for a star to be monoenriched, based on its chemical composition. The majority of stars appear consistent with monoenrichment, with only a small fraction, located to the right of the purple contour, likely being enriched by more than one supernova.

Long-term radial-velocity monitoring for many of these relative bright MP and VMP stars will also prove illuminating.

The authors thank an anonymous referee for positive comments and suggestions that improved the final paper. K.C.R., J.Z., T.C.B., V.M.P., A.F., and S.D. acknowledge partial support from grant PHY 14-30152; Physics Frontier Center/JINA Center for the Evolution of the Elements (JINA-CEE), awarded by the US National Science Foundation. A.F. acknowledges partial support from NSF grant AST-1716251.

Facilities: Southern African Large Telescope (SALT) High Resolution Spectrograph (HRS), Mayall 4 m Telescope, ESO New Technology Telescope.

## **Appendix**

Here we provide the atomic data for lines used in the equivalent-width analysis of the SALT spectra (Table 8).

**Table 8**Line List for Abundances

log gf
-0.890
-0.710
-0.525
-5.688
-0.380
-0.450
-0.239
-0.498

**Note.** Table 8 is published in its entirety in the machine-readable format. A portion is shown here for guidance regarding its form and content.

(This table is available in its entirety in machine-readable form.)

#### **ORCID iDs**

Kaitlin C. Rasmussen https://orcid.org/0000-0002-0470-0800

Joseph Zepeda https://orcid.org/0000-0003-0998-2744
Timothy C. Beers https://orcid.org/0000-0003-4573-6233
Vinicius M. Placco https://orcid.org/0000-0003-4479-1265
Anna Frebel https://orcid.org/0000-0002-2139-7145
Sarah Dietz https://orcid.org/0000-0002-3567-1897
Tilman Hartwig https://orcid.org/0000-0001-6742-8843

#### References

Abate, C., Pols, O. R., Stancliffe, R. J., et al. 2015, A&A, 581, A62 Arcones, A., Janka, H. T., & Scheck, L. 2007, A&A, 467, 1227

Beers, T. C., & Christlieb, N. 2005, ARA&A, 43, 531

Beers, T. C., Lee, Y., Placco, V., & Carollo, D. 2013, AAS Meeting 222, 208.01

Beers, T. C., Placco, V. M., Carollo, D., et al. 2017, ApJ, 835, 81

Beers, T. C., Preston, G. W., & Shectman, S. A. 1992, AJ, 103, 1987

Belokurov, V., Erkal, D., Evans, N. W., Koposov, S. E., & Deason, A. J. 2018, MNRAS, 478, 611

Bisterzo, S., Gallino, R., Straniero, O., Cristallo, S., & Käppeler, F. 2010, MNRAS, 404, 1529

Bovy, J. 2015, ApJS, 216, 29

Bramall, D. G., Schmoll, J., Tyas, L. M. G., et al. 2012, Proc. SPIE, 8446,

Bramall, D. G., Sharples, R., Tyas, L., et al. 2010, Proc. SPIE, 7735, 77354F Bromm, V., & Loeb, A. 2003, Natur, 425, 812

Buckley, D. A. H., Swart, G. P., & Meiring, J. G. 2006, Proc. SPIE, 6267, 626707.

Burris, D. L., Pilachowski, C. A., Armandroff, T. E., et al. 2000, ApJ, 544, 302

Casey, A. R. 2014, PhD thesis, Australian National Univ. Cayrel, R., Hill, V., Beers, T. C., et al. 2001, Natur, 409, 691

Chiaki, G., Tominaga, N., & Nozawa, T. 2017, MNRAS, 472, L115

Chiba, M., & Beers, T. C. 2000, AJ, 119, 2843

Choplin, A., Hirschi, R., Meynet, G., et al. 2018, A&A, 618, A133

Choplin, A., Maeder, A., Meynet, G., & Chiappini, C. 2016, A&A, 593, A36 Côté, B., O'Shea, B. W., Ritter, C., Herwig, F., & Venn, K. A. 2017, ApJ,

Côté, B., Ritter, C., O'Shea, B. W., et al. 2016, ApJ, 824, 82

```
Crause, L. A., Sharples, R. M., Bramall, D. G., et al. 2014, Proc. SPIE, 9147,
Denissenkov, P. A., Herwig, F., Battino, U., et al. 2017, ApJL, 834, L10
Ezzeddine, R., Rasmussen, K., Frebel, A., et al. 2020, ApJ, 898, 150
Frebel, A. 2018, ARNPS, 68, 237
Frebel, A., Casey, A. R., Jacobson, H. R., & Yu, Q. 2013, ApJ, 769, 57
Frebel, A., Johnson, J. L., & Bromm, V. 2007, MNRAS, 380, L40
Hampel, M., Stancliffe, R. J., Lugaro, M., & Meyer, B. S. 2016, ApJ, 831, 171
Hansen, T., Hansen, C. J., Christlieb, N., et al. 2015, ApJ, 807, 173
Hansen, T. T., Holmbeck, E. M., Beers, T. C., et al. 2018, ApJ, 858, 92
Hartwig, T., Yoshida, N., Magg, M., et al. 2018, MNRAS, 478, 1795
Helmi, A., Babusiaux, C., Koppelman, H. H., et al. 2018, Natur, 563, 85
Herwig, F. 2005, ARA&A, 43, 435
Hill, V., Plez, B., Cayrel, R., et al. 2002, A&A, 387, 560
Ishigaki, M. N., Tominaga, N., Kobayashi, C., & Nomoto, K. 2014, ApJL,
   792, L32
Kerr, F. J., & Lynden-Bell, D. 1986, MNRAS, 221, 1023
Kordopatis, G., Gilmore, G., Steinmetz, M., et al. 2013, AJ, 146, 134
Kunder, A., Kordopatis, G., Steinmetz, M., et al. 2017, AJ, 153, 75
Lattimer, J. M., & Schramm, D. N. 1974, ApJL, 192, L145
Lee, Y. S., Beers, T. C., Masseron, T., et al. 2013, AJ, 146, 132
Maeder, A., Meynet, G., & Chiappini, C. 2015, A&A, 576, A56
Meynet, G., Hirschi, R., Ekstrom, S., et al. 2010, A&A, 521, A30
```

Mihalas, D., & Binney, J. 1981, Sci, 214, 829

```
Myeong, G. C., Evans, N. W., Belokurov, V., Sanders, J. L., & Koposov, S. E.
  2018, ApJL, 863, L28
Nomoto, K., Kobayashi, C., & Tominaga, N. 2013, ARA&A, 51, 457
Pignatari, M., Gallino, R., Meynet, G., et al. 2008, ApJL, 687, L95
Placco, V. M., Beers, T. C., Santucci, R. M., et al. 2018, AJ, 155, 256
Placco, V. M., Frebel, A., Beers, T. C., & Stancliffe, R. J. 2014, ApJ, 797, 21
Placco, V. M., Santucci, R. M., Beers, T. C., et al. 2019, ApJ, 870, 122
Roederer, I. U., Preston, G. W., Thompson, I. B., et al. 2014, AJ, 147, 136
Sakari, C. M., Placco, V. M., Farrell, E. M., et al. 2018a, ApJ, 868, 110
Sakari, C. M., Placco, V. M., Hansen, T., et al. 2018b, ApJL, 854, L20
Siegel, D. M., Barnes, J., & Metzger, B. D. 2019, Natur, 569, 241
Sneden, C. A. 1973, PhD thesis, Univ. Texas
Sobeck, J. S., Kraft, R. P., Sneden, C., et al. 2011, AJ, 141, 175
Sommer-Larsen, J., & Zhen, C. 1990, MNRAS, 242, 10
Steinmetz, M., Zwitter, T., Siebert, A., et al. 2006, AJ, 132, 1645
Thielemann, F. K., Eichler, M., Panov, I. V., & Wehmeyer, B. 2017, ARNPS,
  67, 253
Tody, D. 1986, Proc. SPIE, 627, 733
Tody, D. 1993, in ASP Conf. Ser. 52, Astronomical Data Analysis Software
  and Systems II, ed. R. J. Hanisch, R. J. V. Brissenden, & J. Barnes (San
  Francisco, CA: ASP), 173
Yoon, J., Beers, T. C., Dietz, S., et al. 2018, ApJ, 861, 146
Yoon, J., Beers, T. C., Placco, V. M., et al. 2016, ApJ, 833, 20
Yoon, J., Whitten, D. D., Beers, T. C., et al. 2020, ApJ, 894, 7
```